ANNUAL REVIEWS

Annual Review of Nuclear and Particle Science

Photonuclear and Two-Photon Interactions at High-Energy Nuclear Colliders

Spencer R. Klein[1] and Peter Steinberg[2]

[1]Nuclear Science Division, Lawrence Berkeley National Laboratory, Berkeley, California 94720, USA; email: srklein@lbl.gov

[2]Brookhaven National Laboratory, Upton, New York 11973-5000, USA; email: peter.steinberg@bnl.gov

Annu. Rev. Nucl. Part. Sci. 2020. 70:323–54

The *Annual Review of Nuclear and Particle Science* is online at nucl.annualreviews.org

https://doi.org/10.1146/annurev-nucl-030320-033923

Keywords

ultraperipheral collisions, photonuclear interactions, two-photon interactions, heavy-ion collisions, vector mesons, nuclear imaging

Abstract

Ultraperipheral collisions (UPCs) of heavy ions and protons are the energy frontier for electromagnetic interactions. Both photonuclear and two-photon collisions are studied at collision energies that are far higher than those available elsewhere. In this review, we discuss physics topics that can be addressed with UPCs, including nuclear shadowing, nuclear structure, and searches for physics beyond the Standard Model.

Contents

1. INTRODUCTION

Ultraperipheral collisions (UPCs) are collisions of relativistic nuclei (heavy ions or protons) at impact parameters (b) that are large enough that there are no hadronic interactions. Instead, the ions interact electromagnetically via either photonuclear or two-photon interactions. In UPCs, the photons are nearly real, with virtuality $Q^2 < (\hbar/R_A)^2$, where R_A is the nuclear radius. Typical photonuclear interactions include vector meson photoproduction and production of dijets. Typical $\gamma\gamma$ interactions lead to final states such as dileptons, single mesons or meson pairs, or two photons (via light-by-light scattering). **Figure 1** shows some of the reactions discussed in this review. UPCs have previously been reviewed elsewhere (1–6); in this review, we focus on newer developments. We also briefly discuss photoproduction and two-photon interactions in peripheral hadronic collisions.

This review focuses primarily on collisions that involve nuclei and/or protons at Brookhaven's Relativistic Heavy Ion Collider (RHIC) and at CERN's Large Hadron Collider (LHC). The LHC collisions are the energy frontier for photonuclear and two-photon physics, whereas RHIC typically provides higher integrated luminosities and photon energies that are well suited for photonuclear interactions involving reggeon exchange. We also briefly consider collisions at CERN's

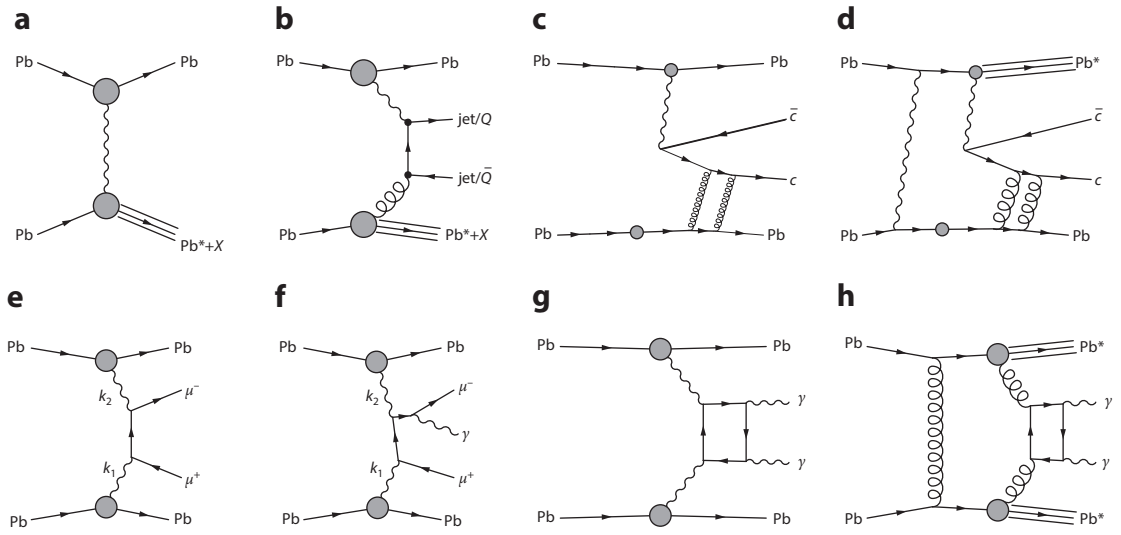

Figure 1

Some of the ultraperipheral collision reactions discussed in this review: (*a*) generic photonuclear interaction with nuclear breakup of the target; (*b*) incoherent photoproduction, generic to heavy quarks and jets; (*c*) exclusive photoproduction of a vector meson; (*d*) coherent photoproduction of a vector meson, accompanied by nuclear breakup; (*e*) dilepton production $\gamma\gamma \to \ell^+\ell^-$; (*f*) dilepton production $\gamma\gamma \to \ell^+\ell^- + \gamma$, including higher-order final-state radiation; (*g*) light-by-light scattering, with no nuclear breakup; and (*h*) central exclusive diphoton production with double breakup.

proposed Future Circular Collider (FCC), China's proposed SPPC (7), and AFTER, a proposed fixed-target experiment using a beam extracted from the LHC (8). AFTER has a lower maximum γp center-of-mass energy ($W_{\gamma p} \approx 2$ GeV/c) but offers higher luminosity. Similar physics is accessible in principle at electron–ion (including proton) colliders, such as EIC, LHeC, and FCC-eh, while two-photon physics can also be studied at e^+e^- colliders. **Table 1** shows the maximum energies for different ion species at these machines. Nuclear beams provide several distinct advantages:

1. A large effective photon luminosity boost proportional to Z^2 for each nucleus, compensating for the overall lower luminosity of nuclear beams
2. Reduced virtuality
3. The possibility of multiphoton exchange between single ions in each beam, allowing for tagging of different impact parameter distributions and photon spectra

Early UPC studies largely focused on e^+e^- pair production and low-energy nuclear physics (1). In the late 1980s, interest grew in using UPCs to probe fundamental physics, most notably two-photon production of the Higgs boson (9, 10). Although the resulting $\gamma\gamma$ luminosities were not encouraging regarding observation of the Higgs boson, they did stimulate work on $\gamma\gamma$ production of other particles. The first calculations of coherent photoproduction with gold beams at RHIC predicted high rates of vector meson photoproduction (11), which were quickly confirmed by the STAR Collaboration (12). The combination of large cross sections and available experimental data stimulated further interest. With the advent of the LHC, the energy reach for UPCs extended dramatically, and the field has blossomed.

Table 1 Capabilities of different colliders

Facility	$\sqrt{s_{NN}}$ or $\sqrt{s_{eN}}$	Maximum E_γ	Maximum $W_{\gamma p}$	Maximum $\sqrt{s_{\gamma\gamma}}$
RHIC (16)				
Au+Au	200 GeV	320 GeV	25 GeV	6 GeV
p+Au	200 GeV	1.5 TeV	52 GeV	30 GeV
pp	500 GeV	20 TeV	200 GeV	150 GeV
LHC (17)				
Pb+Pb	5.1 TeV	250 TeV	700 GeV	170 GeV
p+Pb	8.16 TeV	1.1 PeV	1.5 TeV	840 GeV
pp	14 TeV	16 PeV	5.4 TeV	4.2 TeV
FCC-hh (18), **SPPC** (7)				
Pb+Pb	40 TeV	13 PeV	4.9 TeV	1.2 TeV
p+Pb	57 TeV	58 PeV	10 TeV	6.0 TeV
pp	100 TeV	800 PeV	39 TeV	30 TeV
EIC (19)				
e+Au	89 GeV	4.0 TeV	89 GeV	15 GeV
LHeC (20)				
e+Pb	820 GeV	360 TeV	820 GeV	146 GeV

The table shows the accelerator, ion species, $\sqrt{s_{NN}}$ or $\sqrt{s_{eN}}$, maximum photon energy (in the target rest frame, relevant for cosmic-ray studies), maximum $W_{\gamma p}$ (γp photonuclear center-of-mass energy), and maximum $\gamma\gamma$ energy for two-photon interactions. For the photonuclear interactions, the maximum energies correspond to $x = 1$ in Equation 1 with $b = R_1 + R_2$, the sum of the nuclear radii. For $\gamma\gamma$ interactions, the maximum photon energy is given for $x = 1$ when b is the nuclear radius. For the proton, $r = 0.7$ fm is used; this is similar to treating the proton with a dipole form factor (21). This approach allows photons to carry up to about 30% of the proton's energy—a higher cutoff than was used in some previous works (3). For pA collisions, the maximum $W_{\gamma p}$ is higher when the photons from the proton strike the heavy ion than in the reverse case. The table lists the opposite case because the reaction rate for that direction is usually much higher. For p+Pb at the LHC, the proton and ion beams have different Lorentz boosts, so the per-nucleon center of mass is boosted with respect to the lab frame. For the electron–ion colliders, we use the energies from the cited references (the designs are still evolving, so the beam energies may change), with the same maximum photon energy criteria as for ultraperipheral collisions.

A key to the development of UPCs as a precision laboratory for electromagnetic and strong interaction processes is the development of event generators that simulate both the initial photon flux and the relevant physics processes. The most widely used generator code is STARLIGHT (13), which has been available since the early days of the RHIC program. It implements one- and two-photon processes and includes a set of final states such as vector mesons, meson pairs, and dileptons, with more general photonuclear processes accessible using the DPMJET3 code. The SuperChic 3 Monte Carlo (14) also implements nuclear photon fluxes and computes many of the same processes. Finally, event generators more commonly used for proton–proton reactions, in particular PYTHIA8 (15), implement the coherent photon fluxes required to generate exclusive final states with additional radiative contributions (e.g., QCD jets).

2. THE PHOTON FLUX FROM A RELATIVISTIC ION

2.1. Impact Parameter Dependence

A relativistic ion carries Lorentz-contracted electric and magnetic fields; the electric field radiates outward from the ion, while the magnetic field circles the ion. Fermi (22), von Weizsäcker (23), and Williams (24) showed that these perpendicular fields may be treated as a flux of linearly polarized virtual photons; the energy spectrum is given by the Fourier transform of their spatial (along the ion direction) dependence. In the relativistic limit ($\beta \to 1$) at a distance b from an ion

(where $b > R_A$), the photon energy (k) spectrum from an ion with charge Z, velocity βc, and Lorentz boost γ is

$$N(k,b) = \frac{Z^2\alpha k^2}{\pi^2\gamma^2\hbar^2\beta^2}\left(K_1^2(x) + \frac{K_0^2(x)}{\gamma^2}\right), \quad 1.$$

where K_1 and K_0 are Bessel functions and $x = kb/\beta\gamma\hbar c$. For $x < 1$, $N(k,b) \propto 1/x^2$, while for $x > 1$, the flux is exponentially suppressed. The larger the photon energy, the smaller the range of b that can contribute to the flux.

The values of β and γ are frame-dependent. At colliders, the Lorentz boost of the photon-emitting nucleus in the target rest frame is $\Gamma = 2\gamma^2 - 1$, so photon energies in the PeV range (1 PeV = 10^{15} eV) are accessible in the target rest frame. The target frame is useful for comparison with cosmic-ray air showers.

The total photon flux is found by integrating Equation 1 over b. The integration range depends on the application. For ultraperipheral collisions, to allow for reconstruction of exclusive final states, collisions are excluded in which the nuclei interact hadronically. This can be done by taking the minimum impact parameter $b_{\min}$ to be $2R_A$. The total flux is

$$N(k) = \frac{Z^2\alpha k^2}{\pi^2\gamma^2\hbar^2\beta^2}\left(K_1^2(u) + \frac{K_0^2(u)}{\gamma^2}\right), \quad 2.$$

where $\alpha \approx 1/137$ is the fine-structure constant and $u = \gamma\hbar c/b_{\min} = \gamma\hbar c/2R_A$.

Equation 2 ignores the nuclear skin thickness (about 0.5 fm) and the range of the strong interaction. The flux can be more accurately calculated with

$$N(k) = \int \mathrm{d}^2b N(k,b) P_{0\mathrm{had}}(b), \quad 3.$$

where $P_{0\mathrm{had}}(b)$ is the probability of not having a hadronic interaction. $P_{0\mathrm{had}}(b)$ can be determined with a Glauber calculation (25), which accounts for the nuclear shape and interaction probability. In these calculations, the nucleon distribution of heavy nuclei is well described by a Woods–Saxon distribution, whereas a Gaussian form factor is appropriate for lighter nuclei ($Z \leq 6$) (13). For protons, a dipole form factor is found to work well (21, 26, 27). This corresponds to an exponential charge distribution.

Impact parameter: b_i is the generic distance from one of the ions, while b_1 and b_2 are the distances from each of the two ions; b is the ion–ion impact parameter

Momentum: k is a photon momentum, k_1 and k_2 are the photon momenta in two-photon interactions, q is the exchange gluon/pomeron, and capital P is the momentum of the final state

Momentum transfer: t is the squared momentum transfer, which is q^2 in an elastic process

Pairs: $M_{\ell\ell}$ is the final-state mass for a dilepton state, and $Y_{\ell\ell}$ is the final-state pair rapidity

2.2. Nuclear Dissociation

For heavy nuclei, $Z\alpha \approx 0.6$, so the probability of exchanging more than one photon between the two ions in an individual collision must be considered. These photons are essentially independent of each other even if they are emitted by the same nucleus (28). The additional photons may dissociate one or both nuclei or, less often, introduce additional particles into the detector. Because of the radial dependence of the photon flux, the presence of these additional photons can preferentially select certain impact parameter ranges and thus influence the photon spectrum of the other photons.

Some triggers or analyses may require either the presence or the absence of neutrons in forward zero-degree calorimeters (ZDCs). Additional photons may break up one or both nuclei, producing neutrons. Mutual Coulomb excitation (MCE) via two additional exchanged photons generally leads to neutrons in both ZDCs.

If a harder photon spectrum is desired, one can require neutrons in one or both ZDCs to select events with additional Coulomb excitation—that is, with smaller impact parameters. Adding breakup conditions leads to

$$N(k) = \int \mathrm{d}^2b N(k,b) P_{0\mathrm{had}}(b) P_1(b) P_2(b), \quad 4.$$

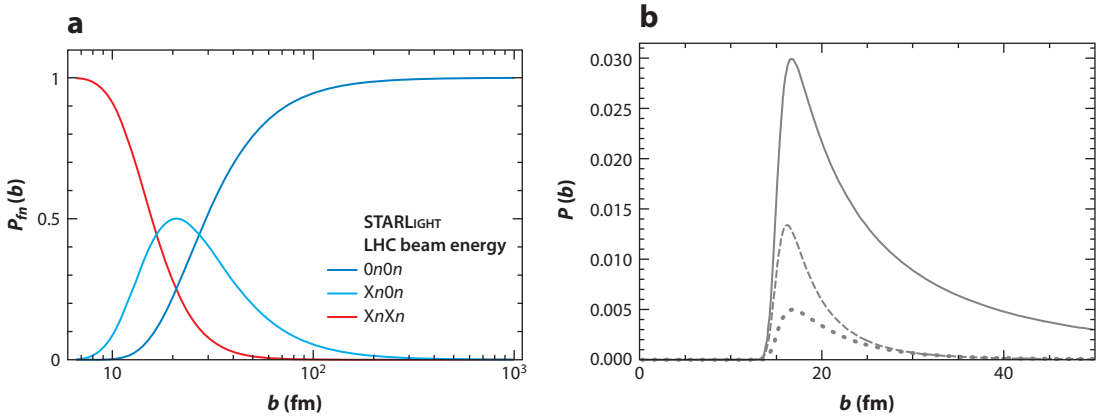

Figure 2

(*a*) Impact parameter dependence of the probabilities, from STARLIGHT, of the three primary forward neutron topologies: 0*n*0*n*, or no neutron emission in either direction, which selects impact parameters $b > 40$ fm; X*n*0*n*, with neutron emission in only one direction, which selects impact parameters of $b \approx 20$ fm; and X*n*X*n*, with neutron emission in both directions, which selects impact parameters $b < 15$ fm. (*b*) STARLIGHT calculation of the impact parameter dependence of coherent ρ production, assuming different zero-degree calorimeter fragmentation scenarios. The difference between mutual Coulomb excitation and no breakup is quite stark at larger impact parameters. Panel *b* data from Reference 29.

where P_1 and P_2 are the excitation probabilities for the two nuclei. In general, $P_i(b) \propto 1/b^2$, so requiring nuclear excitation leads to smaller impact parameters. This is demonstrated using STARLIGHT for the three possible cases in **Figure 2*a***, which shows the functional forms of $P_{fn}(b)$, the impact parameter–dependent probability of a particular forward neutron configuration: X*n*X*n* $[P_1(b)P_2(b)]$, X*n*0*n* $[(1 - P_1)P_2 + (1 - P_2)P_1]$, and 0*n*0*n* $[(1 - P_1)(1 - P_2)]$. Calculations from Reference 29, shown in **Figure 2*b***, demonstrate the stark differences in the impact parameter dependence of ρ photoproduction for different ZDC topologies (in this case, X*n*X*n*, 1*n*1*n*, and 0*n*0*n*) for collisions at RHIC.

Equation 4 can also be applied to meson photoproduction. At the LHC, when $b = 2R_A$, the probability of producing a ρ^0 is about 3%; assuming that the electromagnetic fields are not depleted, the probability of ρ photoproduction should be Poisson distributed, so the probability of producing two ρ^0 is about 5×10^{-4}. These probabilities translate to roughly one million pairs in a 1-month LHC heavy-ion run (11). More exotic pairs, such as $\rho J/\psi$, should also be visible. These pairs are of interest because the two vector mesons should share a common polarization (28). Since they are bosons, there should be an enhanced probability of producing the two mesons in the same final state and, potentially, of observing stimulated decays.

For some applications, the photon flux within the nucleus ($b < R_A$) is of interest. Two examples are $\gamma\gamma$ production of lepton pairs—which may occur within one of the nuclei (without dissociating it), even when $b > 2R_A$—and the study of electromagnetic processes in peripheral collisions, in which there are also hadronic interactions. At transverse distance $b_i < R_A$ from the nuclear center, only nucleons in a cylinder with radius b_i contribute coherently to the interaction (30). This constraint can be included by adding a form factor to the photon emission flux (31–33). It is also possible that the hadronic interaction might disrupt the coherent photon emission. However, because the photons are nearly real, they should be mostly emitted at a time before the hadronic interaction occurs.

2.3. k_T Spectrum

The photon k_T spectrum can be derived from the equivalent photon approximation (EPA). If one integrates the photon flux over all b, then the photon k_T may be determined exactly (31):

$$\frac{\mathrm{d}^2N}{\mathrm{d}^2k_T} = \frac{\alpha Z^2 F(k_T^2 + k_z^2/\gamma^2)k_T^2}{\pi^2(k_T^2 + k_z^2)^2}, \qquad 5.$$

where $F(k^2)$ is the nuclear form factor. When integrated over k_T, this gives Equation 3.

If the range of b is restricted, such as by requiring $b > 2R_A$ or by weighting the b distribution by the requirement that an additional photon or photons be exchanged, the problem becomes much more complicated because k_T and b are conjugate variables. This is seen in more complete quantum electrodynamics (QED) calculations (e.g., 31, 33). As the range of b is restricted, the mean k_T should increase. Unfortunately, there is no method available to calculate the k_T spectrum for these cases. Calculations for two-photon interactions are more complicated because the $\gamma\gamma$ interaction point is distinct from the radial positions relative to each of the two nuclei. In principle, restrictions on the ion–ion impact parameter do not affect the photon p_T spectrum at this third point. However, final states clearly identified with $\gamma\gamma \to \ell^+\ell^-$ show significant k_T broadening as the impact parameter range is restricted to smaller values in hadronic heavy-ion collisions (34–36), as we discuss below.

2.4. Uncertainties on the Photon Flux

The photon flux calculations are subject to a number of theoretical uncertainties:

1. Overlap condition: The implementation of $P_{0\mathrm{had}}$ is straightforward, but it uses optical Glauber calculations, which are known to be limited in applicability.
2. Restriction on production points: It is typically assumed that UPC processes cannot originate within a nucleus (i.e., $b_i > R_i$), but this has not been clearly established using data. It is possible that some range within a nucleus could be accessible to these processes, contributing to the observed enhancement of J/ψ in peripheral collisions.
3. Assumption of a uniform flux: Normally, the photon flux is taken to be constant across the entire target nucleus, which is well represented by a plane wave. This assumption ignores the fact that the maximum photon energy (and flux) is higher on the near side of the nucleus and lower on the far side.

For two-photon interactions, the effect of changing impact parameter cutoffs has been studied. The uncertainty rises with increasing $W_{\gamma\gamma}/\sqrt{s_{NN}}$, reaching about 5% at half of the maximum $W_{\gamma\gamma}$ shown in **Table 1** (37). For the other uncertainties, precise experimental measurements are required to assess their relative importance.

3. PHOTOPRODUCTION PROCESSES: γp AND γA

3.1. Low-Energy Photonuclear Interactions (Including Nuclear Dissociation)

Because the photon spectrum scales roughly as $1/k$, the most common photonuclear interactions involve low-energy nuclear excitations. The Coulomb excitation with the largest cross section is the giant dipole resonance (GDR). In it, protons and neutrons oscillate collectively, against each other (38). The GDR has the same quantum numbers as the photon $J^{PC} = 1^{--}$, so it is readily produced by photoexcitation. GDRs decay primarily by single neutron emission, whereas most higher excitations involve the emission of multiple neutrons. For this reason, the GDR provides a

useful calibration signal. The total excitation cross section is determined by combining the photon spectrum with the photonuclear excitation cross section:

$$\sigma(\text{excitation}) = \int \mathrm{d}k \frac{\mathrm{d}N}{\mathrm{d}k} \sigma(\gamma A \to A^{\star}). \quad 6.$$

$\sigma(\gamma A \to A^{\star})$ is determined from a compilation of photoexcitation data (39) or, in some cases, from first principles (40). Because these cross sections can be very large, corrections may be needed to account for unitarity; without such corrections, $P_i(b)$ can be large for $b \approx 2R_A$ (39). Multiple photon absorption leads to higher excitations. The Coulomb excitation cross section is about 95 barns with gold–gold collisions at RHIC and 220 barns with lead–lead collisions at the LHC.

Interactions with different requirements on nuclear breakup (or nonbreakup, where no observed neutrons are required) can be calculated in an impact parameter–dependent formalism. For example, MCE primarily occurs via two-photon exchange, with each photon exciting one nucleus. The cross section for MCE is

$$\sigma(\mathrm{X}n\mathrm{X}n) = \int \mathrm{d}^2 b P_1(b) P_2(b) P_{0\mathrm{had}}(b), \quad 7.$$

where the respective probabilities are for exciting nucleus 1, exciting nucleus 2, and not having a hadronic interaction. The excitation probabilities can be determined from Equation 6, using the impact parameter–dependent photon flux.

MCE can be used to monitor luminosity. The most delicate part is accurately determining $P_{0\mathrm{had}}(b)$ when $b \approx 2R_A$. This uncertainty can be avoided by instead calculating and measuring the summed cross section for MCE plus hadronic interactions (41). Alternatively, events with one neutron in each ZDC generally correspond to mutual GDR excitation, which has lower backgrounds from hadronic interaction than does MCE in general (42); however, the cross sections are lower, so the statistics are limited.

The neutron multiplicity distribution in Coulomb exchange processes has been studied by several groups (43)—most recently by the ALICE Collaboration (44), whose ZDCs could separate events containing one to four neutrons. Their measurements were in generally good agreement with the predictions of the RELDIS model (40). RELDIS uses the Weizsäcker–Williams photon flux, measured photonuclear cross sections, and neutron emission via cascade and evaporation codes. The $\mathrm{n}_0^0\mathrm{n}$ afterburner (45) performs similar calculations but in a Monte Carlo format that can be used with existing simulations to simulate vector meson photoproduction with nuclear breakup.

3.2. Probing Nuclear Parton Distributions with Incoherent Photoproduction

As **Figure 1*b*** shows, the photon–gluon fusion process directly probes the gluons in the oncoming nucleus, so it can be used to directly study nuclear shadowing (46). Triggering on such processes is aided by the fact that the photon emitter typically does not break up. However, the recoiling partons will in general excite the nucleus, leading to nuclear dissociation and an accompanying partonic color connection between the reaction products and the nuclear remnants.

This process leads to a distinct event signature (with limited transverse energy, neutrons in only one direction, and one or more reconstructed jets), which can be easily selected by an experimental trigger. **Figure 3*a*** shows an example event that is triggered using an exclusive one-arm ZDC trigger and that contains two forward reconstructed jets.

Jets are straightforward to reconstruct, in particular in low-multiplicity photonuclear events, but the condition of being well reconstructed imposes a minimum p_{T}, which restricts the kinematic coverage in Bjorken-x (the fraction of the nucleon momentum) and Q^2 (the hardness scale

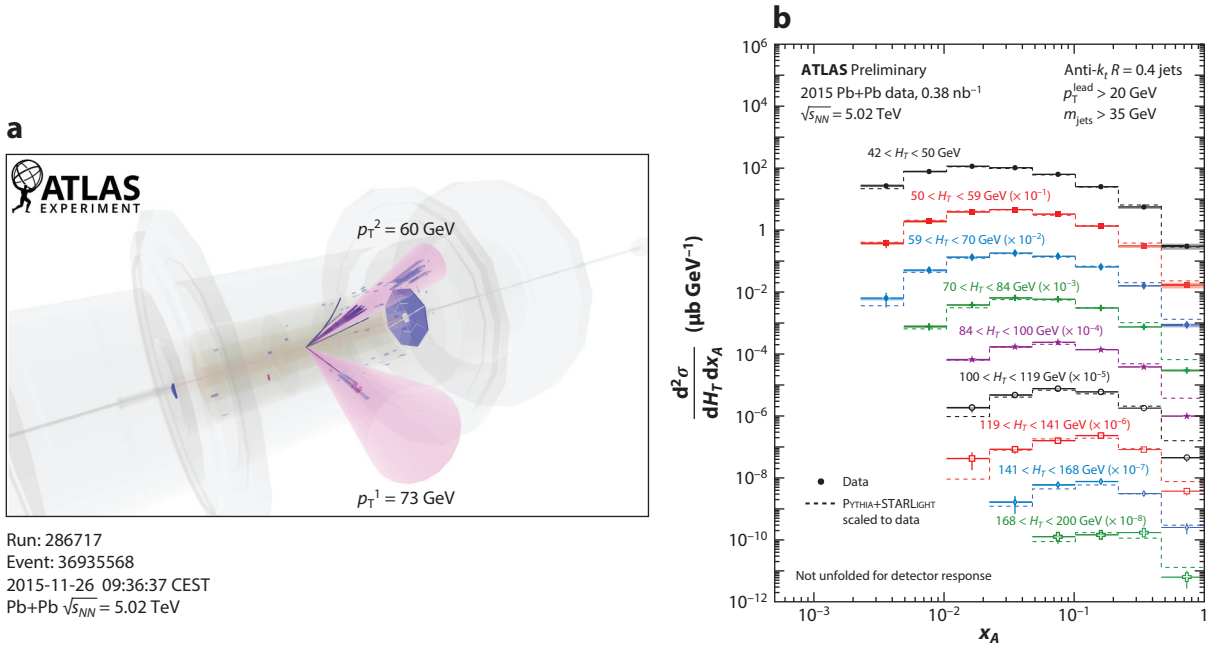

Figure 3

(*a*) Example event with a large gap in one direction and two jets in the other direction. Panel adapted from Reference 46a (CC BY 4.0). (*b*) Uncorrected triple-differential cross sections for photonuclear dijet production, presented as a function of the per-nucleon momentum fraction x_A in selections of the scalar p_T sum H_T. Panel adapted from Reference 47 (CC BY 4.0).

of the interaction). ATLAS has presented preliminary triple-differential quasi-cross sections that are corrected for trigger efficiency but not yet unfolded for experimental resolution (47). The experimental variables are H_T, the scalar sum of the observed jet transverse momenta; z_γ, which reflects the energy fraction of the incoming nucleon energy carried by the photon; and x_A, the per-nucleon momentum fraction in the struck nucleus. The data are compared with those from a PYTHIA6 photoproduction calculation, with the photon spectrum taken from STARLIGHT. The particular result shown in **Figure 3*b*** shows cross sections versus x_A for selections in H_T. Although the data have not yet been compared in detail with PYTHIA data, the general agreement is very promising.

Photoproduction of open charm also proceeds via photon–gluon fusion. Open charm can be detected relatively near threshold ($M_{c\bar{c}} \approx$ a few times m_c), so it can probe lower x and Q^2 gluons than dijets (48). Charmed quarks, with a charge of $+2/3e$, have a particularly large cross section (49, 50). The disadvantage is that charm quarks can hadronize to several different hadrons, each with several possible final states. Many of the final states are difficult to reconstruct, so the overall reconstruction efficiency is small. Open bottom should also be visible at rates high enough for parton distribution studies (51), and top quark pair production may be accessible in pA collisions at the LHC (52, 53).

Inelastic photoproduction is a topic of interest in its own right. Proceeding by the fluctuation of the photon to a hadronic state, typically a ρ meson, it provides another example of collective behavior in small systems. Early results from ATLAS (54) indicate that these collisions show a ridge-like structure in the two-particle azimuthal correlation function—similar to that seen in pp

but with a smaller magnitude—possibly reflecting a more compact quark–antiquark configuration compared with the proton with its three constituent quarks.

3.3. Coherent and Incoherent Photoproduction of Vector Mesons

Vector meson production may occur either coherently, in which case the target nucleus remains intact, or incoherently, which means that the nucleus has been excited or dissociated.

3.3.1. Coherent photoproduction. Coherent photoproduction cannot involve color exchange, so it must proceed via the exchange of at least two gluons. At high energies, this two-gluon exchange is often referred to as a pomeron exchange. The pomeron has the same quantum numbers as the vacuum, $J^{PC} = 0^{++}$, so it can be described as representing the absorptive part of the cross section (55). At lower photon energies, meson photoproduction can also proceed via reggeon exchange, in which the reggeons represent collective meson trajectories. Reggeons carry a much wider range of quantum numbers than the pomeron does, and they can be either neutral or charged. Thus, the range of final-state spin and parity is much wider, and charged final states and exotica are possible. In UPCs, lower photon energy corresponds to production at forward rapidities, so this physics can best be studied with forward spectrometers.

The vector meson rapidity distribution $d\sigma/dy$ can be converted to the incoming lab-frame photon and pomeron energy via the relationships

$$k_{1,2} = \frac{M_V}{2} e^{\pm y}, \quad q_{1,2} = \frac{M_V}{2} e^{\mp y}, \tag{8.}$$

where M_V is the vector meson mass; we neglect the k_T and q_T. The $\pm$ and $\mp$ signs arise from the twofold ambiguity over which nucleus emitted the photon. Away from $y = 0$, the two possibilities have different photon and pomeron energies. This degeneracy complicates the extraction of energy-dependent photoproduction cross sections. It can be largely avoided in pA or other asymmetric collisions, in which the photon comes predominantly from the heavy ion with the proton as a target (56–58). Unfortunately, pA collisions do not allow us to effectively probe ion targets. For pp collisions, HERA data can be used to fix the cross section for one of the photon directions, allowing the cross section for the other direction to be found (59). For ion–ion collisions, another strategy is required: selecting sets of events with different photon spectra, leading to different ratios for production in the two directions. This strategy can be implemented by selecting sets of events with different impact parameter distributions. For example, events accompanied by MCE have a harder photon energy spectrum (28, 29). Another option is to compare photoproduction in peripheral and ultraperipheral collisions (60). By using multiple data sets with different impact parameter distributions, it is possible to unambiguously find the energy dependence of the cross section $\sigma(k)$, albeit with increased errors due to the coupled equations.

3.3.2. Cross section for γp interactions. The bidirectional ambiguity problem goes beyond summing the cross sections for the two photon directions. For coherent photoproduction, the reactions with different photon directions are indistinguishable, so they interfere with each other (61). The sign of the interference depends on how the two possibilities are related. A reaction in which ion 1 emits a photon can be transformed into a reaction in which ion 2 emits a photon by a parity exchange. Vector mesons have negative parity, so the interference is destructive. For $\bar{p}p$ collisions at the Fermilab Tevatron, the relevant symmetry is CP, so the interference is constructive.

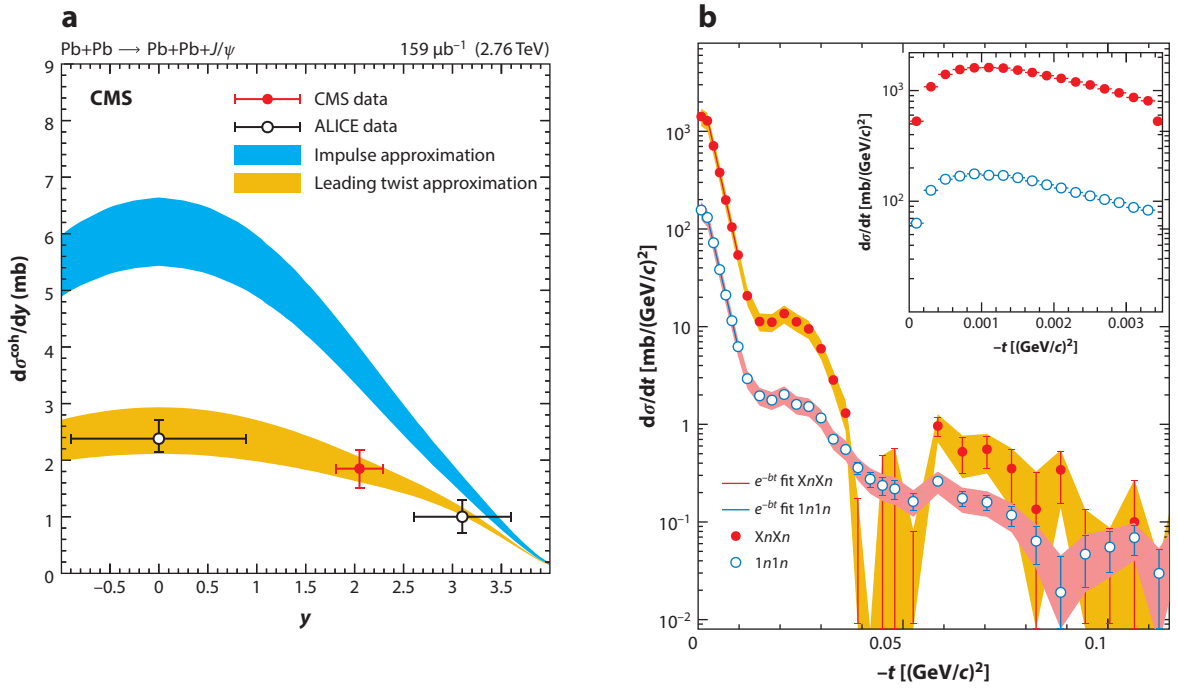

Figure 4

(*a*) CMS and ALICE measurements of J/ψ $d\sigma/dy$ as a function of rapidity, based on LHC Run 1 data. Panel adapted from Reference 76 (CC BY 4.0). (*b*) $d\sigma/dt$ for ρ^0 photoproduction in gold–gold collisions at a center-of-mass energy of 200 GeV per nucleon as measured by the STAR Collaboration. These data are for ρ photoproduction accompanied by mutual Coulomb excitation; the two curves are for different selections of numbers of neutrons in each zero-degree calorimeter. The inset shows $d\sigma/dt$ at very low t, where interference between the two directions is visible. Panel adapted with permission from Reference 42.

There is also a propagator $\exp(i\vec{p}_T \cdot \vec{b})$ present. For an interaction at a given impact parameter,

$$\frac{d^2\sigma}{dbdy} = \left|A_1(b,k_1) - e^{i\vec{p}_T\cdot\vec{b}}A_2(b,k_2)\right|^2, \qquad 9.$$

where $A_1(b, k_1)$ and $A_2(b, k_2)$ are the amplitudes for the two directions. When $y \approx 0$, in the limit $p_T \to 0$, interference is complete and $\sigma \to 0$. Away from $y = 0$, the photon energies corresponding to the two directions are different, so $A_1(b, k_1)$ and $A_2(b, k_2)$ are different, reducing the degree of interference. When $p_T \gg \hbar/R_A$, the propagator oscillates rapidly with small changes in b and thus averages out. Because of the oscillatory behavior, this interference does not significantly affect the total cross section. As the inset in **Figure 4*b*** shows, suppression is visible for $p_T < 30$ MeV (42) at the expected level (62).

One interesting aspect of this interference is that the production amplitudes at the two nuclei are physically separated and share no common history. Moreover, the two vector meson amplitudes decay almost immediately. The ρ^0 has a lifetime of order 10^{-23} s, producing two pions that travel in opposite directions. These pions become physically separated long before the wave functions for production at the two ions can overlap. With the interference-imposed requirement that the pair p_T not be zero, the pion pair can only be described with a nonlocal wave function. This is an example of the Einstein–Podolsky–Rosen paradox (63).

γp interactions have been extensively studied at fixed-target experiments (64) and the HERA ep collider (65). A wide range of final states have been observed. At high energies, pomeron exchange

dominates, and the most common final states are vector mesons, including the ρ, ω, ϕ, J/ψ, ψ', and Υ states. Direct $\pi^+\pi^-$ pairs are also produced. Their production may be modeled as photon fluctuations directly to a pair of charged pions.

The cross section to produce a vector meson V depends on the probability of the photon fluctuating to a $q\bar{q}$ pair and on the cross section for that pair scattering elastically from the target, emerging as a real vector meson. The fluctuation probability depends on the quark charge and vector meson wave function; it is quantified with the coupling f_v, which is determined from Γ_{ll}, the leptonic partial width for $V \to e^+e^-$. The elastic scattering cross sections are then determined using $\sigma(\gamma p \to Vp)$ and f_v.

In lowest-order perturbative QCD (pQCD), the reaction proceeds via two-gluon exchange. Two gluons are required to preserve color neutrality. The forward scattering cross section to produce a vector meson with mass M_V is often given as (66)

$$\left.\frac{\mathrm{d}\sigma}{\mathrm{d}t}\right|_{t=0} = \frac{\Gamma_{ll} M_v^3 \pi^3}{48\alpha}\left[\frac{\alpha_S(\overline{Q}^2)}{\overline{Q}^4} xg(x,\overline{Q}^2)^2\left(\frac{1+Q^2}{M_V^2}\right)\right], \qquad 10.$$

where α_S is the strong coupling constant; x is the Bjorken-x of the gluon; and $\overline{Q}^2 = (Q^2 + M_V^2)/4$, where Q is the photon virtuality, which is generally small. The division by four is necessary because there are two gluons, each assumed to carry half the virtuality; as discussed below, this assumption is problematic. The vector meson mass provides a hard scale that allows the use of pQCD even when the photon virtuality is small. pQCD is usually assumed to be applicable for photoproduction of the J/ψ and heavier mesons. Two gluons form the simplest color-neutral object that can be exchanged. More sophisticated models treat pomeron exchange as a gluon ladder (67).

The two-gluon approach has some important caveats (68), many of which also apply to incoherent photoproduction. The gluon density, $g(x, \overline{Q}^2)$, is squared to account for the two gluons, but there is no reason that the two gluons should have the same x and Q^2 values. In fact, the largest contribution occurs when the two gluons have very different x values, $x_1 \gg x_2$, so the softer gluon is relatively unimportant. One way to account for the soft gluon is to treat the interaction using a generalized parton distribution (GPD). Another approach is to account for the second gluon using a Shuvaev transformation (69), which leads to a multiplicative factor as in Equation 10. As long as $x_1 \gg x_2$, the Bjorken-x of the dominant gluon can be related to the pomeron energy from Equation 8 via $x = q/m_p = M_V/m_p \exp(\mp y)$, where m_p is the proton mass.

There are also small corrections to account for higher-order photon fluctuations (resolved photons), such as to $q\bar{q}g$. Finally, there is some uncertainty due to the choice of mass scale, $\mu = \overline{Q}$, used to evaluate the gluon distribution (66). All of these considerations are the subject of intense theoretical discussion (70). One important next step is to extend the calculation to next-to-leading order (NLO). There is not yet a complete NLO calculation, but most of the elements exist, and there are several partial-NLO results.

The NLO calculation includes contributions from many Feynman diagrams, including several in which the quark distributions in the target are important. A problem arises with the NLO calculation, at least at LHC energies: The NLO amplitude is larger than the leading-order (LO) amplitude. This problem is due to the parton distributions used as input. There are no gluon data in this x, Q^2 range, so the parton distributions extrapolate downward in x, finding a very small gluon contribution. This leads to a very small LO cross section, so it is unsurprising that the NLO diagrams give a larger contribution. By starting with a larger gluon contribution, such as can be inferred from the J/ψ coherent photoproduction data, this problem disappears.

The cross section is sensitive to the choice of factorization and renormalization scales and to the choice of minimum virtuality to consider. This sensitivity can be reduced with a careful choice

of minimum virtuality, Q_0 (71). With an optimal choice, the scale uncertainty is reduced to a range of ±15% to ±25% for the Υ and to a somewhat larger range for the J/ψ. This range is not small, but it is small enough to allow photoproduction to meaningfully contribute to parton distribution fits in this x, Q^2 range even with the systematic uncertainties (72).

The longitudinal momentum transfer q_z in photoproduction is determined by the kinematics: $q_z = 4k/M_V^2$. The maximum momentum transfer is set by the coherence condition applied to the proton size R_p, $q < \hbar/R_p$. More precisely, the p_T is regulated by the proton form factor, and the cross section can be written as

$$\sigma(\gamma p \to Vp) = \left.\frac{d\sigma}{dt}\right|_{t=0} \int_{t_{min}}^{\infty} |F(t)|^2 dt, \qquad 11.$$

where $t \approx p_T^2$, $F(t)$ is the proton form factor, and t_{min} is the minimum momentum transfer, $M_V^2/2k$ (with k in the target frame). $d\sigma/dt|_{t=0}$ encodes all of the hadronic physics of the reaction. Because Equation 10 is decoupled from the nuclear form factor in Equation 11, in this approach, changes in the gluon distribution do not alter the nuclear shape.

Several groups have used UPCs to study J/ψ photoproduction on proton targets, extending the data collected at HERA. Above the threshold region, HERA and fixed-target experiments found that the J/ψ photoproduction cross section is well described by a power law $\sigma \propto W_{\gamma p}^{\alpha}$, with $\alpha = 0.67 \pm 0.03$ (59). This linear relationship is expected in LO pQCD (Equation 10) as long as the low-x gluon distribution itself follows a power law, $g(x, Q^2) \propto x^{-\alpha/2}$. A deviation from this power law would signal that higher-order diagrams are becoming important—a possible precursor to saturation. The ALICE collaboration used p+Pb collisions to extend the measurement up to roughly $W_{\gamma p} = 800$ GeV, probing gluons with $x \approx 2 \times 10^{-5}$ and finding no deviation from the power-law behavior (73). In the overlap region, the ALICE data were in good agreement with the HERA data. It should be noted that at these energies, NLO calculations predict J/ψ cross sections similar to those predicted by LO calculations.

The LHCb Collaboration conducted a similar study of pp collisions at $\sqrt{s} = 7$ TeV and $\sqrt{s} = 13$ TeV (59). They used HERA data to fix the cross section in the direction corresponding to the low-energy photon solution and then solved for the cross section in the high-energy photon direction. At $\sqrt{s} = 13$ TeV, their highest rapidity point, $\langle y \rangle = 4.37$ corresponded to $W_{\gamma p} \approx 1.7$ TeV and $x \approx 3 \times 10^{-6}$. Unfortunately, the results from the different energies show some tension. The data for $\sqrt{s} = 7$ TeV follow the HERA power law, whereas the data for $\sqrt{s} = 13$ TeV are lower, consistent with an NLO prediction. The LHCb Collaboration found similar power-law behavior for the ψ', albeit with larger statistical uncertainty (74).

The Υ states are of interest because the LO and NLO calculations differ more in particular with increasing collision energy, making them more sensitive to the presence of higher-order contributions (66). LHCb has also observed photoproduction of the three Υ states (74). For the Υ(1S) state, where the statistics are best, the LHCb Collaboration observed good agreement with their NLO calculations, above the LO predictions.

The CMS Collaboration studied ρ photoproduction on protons in p+Pb collisions, focusing on the p_T spectrum. They showed a pion-pair p_T spectrum out to 1 GeV/c (57) and found that it was well described by a mixture of exclusive interactions, so-called incoherent interactions in which the proton dissociated, and $\rho^0(770)$ feed-down from $\rho(1700)$ decays. From this observation, they extracted the $\rho(770)$ component of the dipion spectrum and found that the cross section was in agreement with HERA predictions but that $d\sigma/dt$ dropped faster than an exponential. Their data were well fitted by the form $\exp(-bt + ct^2)$, with $c \approx 3\sigma$ from zero, which indicates that the proton size depends on the Q^2 at which it is observed.

CMS used a similar technique to study the Υ states in p+Pb collisions (56). They resolved the $\Upsilon(1S)$ and $\Upsilon(2S)$ peaks and concentrated on the $\Upsilon(1S)$ state, where the statistics were better. Because of the scaling with Z, the continuum background from $\gamma\gamma \to \mu\mu$ was substantially larger in these p+Pb collisions than in pp collisions. The cross section was consistent with a power law in $W_{\gamma p}$, at a level between the NLO and LO predictions shown by CMS.

3.3.3. Cross section for γA interactions. One issue driving studies of vector meson photoproduction in γA is how the parton distributions in nucleons change when they are embedded in nuclei—a phenomenon known as nuclear shadowing. If shadowing is ignored, the cross section may be found via a Glauber calculation (75):

$$\frac{\mathrm{d}\sigma_{\gamma A\to VA}}{\mathrm{d}t} = \left.\frac{\mathrm{d}\sigma_{\gamma p\to Vp}}{\mathrm{d}t}\right|_{t=0} \left| \int \mathrm{d}^2 b \int \mathrm{d}z e^{i(\vec{q_t}\cdot\vec{b}+q_l z)} \rho(b,z) e^{-\frac{1}{2}\sigma_{\mathrm{tot}}(Vp)T_A(b,z)} \right|^2, \qquad 12.$$

where

$$T_A(z) = \int_z^\infty \rho(b,z')\mathrm{d}z' \qquad 13.$$

and $\rho(b, z)$ is the nuclear density. $\sigma_{\mathrm{tot}}(Vp)$ is the total vector meson–nucleon cross section, determined using the optical theorem:

$$\sigma_{\mathrm{tot}}^2(Vp) = 16\pi \left.\frac{\mathrm{d}\sigma(Vp\to Vp)}{\mathrm{d}t}\right|_{t=0}. \qquad 14.$$

Here, the elastic scattering cross section $\mathrm{d}\sigma(Vp \to Vp)/\mathrm{d}t$ is determined from the measured photoproduction cross section after factoring out the $\gamma \to V$ fluctuation probability. The exponential $\exp(i(\vec{q_t}\cdot\vec{b} + q_l z))$ accounts for coherence across the nucleus.

The Glauber calculation accounts for multiple interactions—a single dipole encountering a nucleus may interact more than once but can produce only a single vector meson. For small $\sigma_{\mathrm{tot}}(Vp)$ (i.e., heavy mesons like the J/ψ), multiple interactions are unlikely, the amplitudes add linearly, and the forward cross section $\mathrm{d}\sigma/\mathrm{d}t|t = 0$ scales as A^2. Light mesons, with large $\sigma_{\mathrm{tot}}(Vp)$, will interact on the front surface of the target nucleus, so the amplitude depends on the frontal surface area of the target, which scales as $A^{2/3}$, and $\mathrm{d}\sigma/\mathrm{d}t|_{t=0} \propto A^{4/3}$. The Glauber calculation accurately interpolates between these limits under the assumption that the γp cross section is the same for isolated protons and for those in nuclei. The range of t for which coherent photoproduction is possible decreases as $A^{-2/3}$, moderating the increase in total coherent cross section. If significant shadowing is present, then the cross section is reduced below the Glauber expectation. For heavy nuclei at RHIC/LHC energies, the resulting cross section is only slightly dependent on the photon energy, even if the γp cross section shows a significant photon energy dependence.

With these caveats in mind, it is useful to compare the heavy-ion data with pQCD calculations. **Figure 4*a*** shows CMS central and ALICE forward muon spectrometer data on $\mathrm{d}\sigma/\mathrm{d}y$ for J/ψ photoproduction on a lead target. The measurements from both collaborations are about a factor of two below the impulse approximation, which treats the lead nucleus as a collection of free nucleons. The data are, however, consistent with a leading twist pQCD calculation (77, 78), which is essentially an extension of the Glauber calculation discussed above that accounts for the possibility of the incident quark and antiquark to interact multiple times while traversing the nucleus, including excited intermediate states. The Glauber calculation treats shadowing as due to multiple scattering. It will be very interesting to see data on shadowing in Υ photoproduction, in which the Q^2 is larger. Unfortunately, the larger background from $\gamma\gamma \to \ell^+\ell^-$ will be a bigger problem than in p+Pb or pp collisions.

For lighter mesons, like the ρ and ω, the Q^2 is low enough that pQCD is not expected to be applicable. One can use γp data to predict the γA cross sections with a Glauber calculation (75), as described above. Experiments have observed a dipion mass spectrum with three components: $\rho^0 \to \pi^+\pi^-$, $\omega \to \pi^+\pi^-$, and direct $\pi^+\pi^-$ production. These three channels are indistinguishable, so they all interfere with each other. The direct $\pi^+\pi^-$ is flat independent of mass, but, through interference, it enhances the $\pi^+\pi^-$ spectrum below the ρ mass and depletes the spectrum above it. The branching ratio for $\omega \to \pi^+\pi^-$ is only 2.2%, but, through its interference with the ρ meson, the ω meson produces a kink in the mass spectrum near the ω mass (42, 57). The relative amplitudes of the three channels seem consistent with HERA data. Surprisingly, data on ρ photoproduction from both STAR (79) and ALICE (80) show a ρ cross section that is larger than that predicted by Glauber calculations (Equation 12). One possibility is that nuclear inelastic scattering (by intermediate higher-mass photon fluctuations) increases in the cross section (81).

Photoproduction can also be used for vector meson spectroscopy. Although meson photoproduction has long been studied in fixed-target experiments (64) and at HERA, current UPC analyses have collected large data samples (up to about one million events) with high-quality detectors—comparable in size and with larger maximum mass reach than fixed-target experiments—and are starting to produce interesting results. STAR has observed a $\pi^+\pi^-$ resonance with a mass around 1.65 GeV and a width around 165 MeV (82). The rate appears roughly consistent with photoproduction of the $\rho_3(1690)$. If eventually verified, by STAR or a future experiment, to be the $\rho_3(1690)$, this would be an interesting observation of a spin-3 meson at a $W_{\gamma p}$ where production via pomeron exchange dominates. STAR (83) and ALICE (84) have also studied photoproduction of $\pi^+\pi^-\pi^+\pi^-$ final states and have observed a broad resonance that seems consistent with a mixture of the $\rho(1450)$ and $\rho(1700)$ states. Data that have been collected but not yet analyzed could be used to significantly improve our knowledge of heavier vector meson states.

3.4. The Dipole Model and Nuclear Imaging with Coherent Photoproduction

An alternative approach to vector meson photoproduction treats the interacting photon as a quark–antiquark dipole with separation r_T. This dipole may scatter in the target, emerging as a vector meson. This approach treats protons and ions in a similar manner, via a target configuration Ω that describes positions of the gluons in the target. It meshes smoothly with the Good–Walker approach to diffraction (85), thus allowing calculations of incoherent photoproduction. The cross section to produce a vector meson is (46, 86, 87)

$$\frac{\mathrm{d}\sigma}{\mathrm{d}t} = \frac{1}{16\pi}\left|A^{\gamma A \to VA}\right|^2(1+\beta^2), \qquad 15.$$

where

$$A^{\gamma A \to VA} = i\int \mathrm{d}^2\vec{r}_T \int \frac{\mathrm{d}z}{4\pi}\int \mathrm{d}^2\vec{b}_T\,\psi^*_\gamma(\vec{r}_T,z,Q^2)N_\Omega(\vec{r}_T,\vec{b}_T)\psi_V(\vec{r}_T,z,Q^2)e^{-i\vec{b}_T\cdot\vec{k}_T/\hbar}, \qquad 16.$$

where $\vec{b}_T$ is the transverse position within the nucleus, $\vec{r}_T$ is the transverse size of the dipole, z is the fraction of the photon momentum carried by the quark (the antiquark has momentum fraction $1-z$), and Q^2 is the photon virtuality. The wave function of the incident photon, $\psi^*_\gamma(\vec{r}_T,z,Q^2)$, includes the probability of the photon fluctuating to a dipole. This probability is related to Γ_{ll}. The wave function includes the probability distribution for the quark to carry a momentum fraction z. This probability is symmetric around $z = 0.5$ and is weighted toward low-mass dipoles, where $z \approx 0.5$.

Different models have been used for the wave function of the outgoing vector meson, $\psi_V(\vec{r}_T,z,Q^2)$ (88). Quark models indicate that it should be Gaussian in $\vec{r}_T$. The Gaussian light

cone form is

$$\psi_V(\vec{r}_T, z, Q^2) = N[z(1-z)]^2 e^{-R_T^2/\sigma^2}, \quad 17.$$

where the normalization N and width σ are based on fits to data. The boosted Gaussian is slightly more complex, as it is based on the Fourier transform of the (momentum-space) light cone wave function.

Here, $N_\Omega(\vec{r}_T, \vec{b}_T)$ is the imaginary part of the forward dipole-target scattering amplitude for a dipole with transverse size $\vec{r}_T$, impacting the target at transverse position $\vec{b}_T$. The small real part of the amplitude is accounted for by the $(1 + \beta^2)$ term in Equation 15. The subscript Ω denotes the target configuration (nucleon positions, etc.). This formulation assumes that the dipole size is smaller than the nuclear target; if the dipole is larger, the exponential becomes slightly more complicated.

The optical theorem provides a simple relationship with the dipole scattering cross section: $N_\Omega(\vec{r}_T, \vec{b}_T) = \mathrm{d}^2\sigma_{q\bar{q}}/\mathrm{d}^2 b$. In a pQCD context, the cross section depends on the gluon density $g(x, \mu^2)$ (89)

$$\frac{\mathrm{d}^2\sigma_{q\bar{q}}}{\mathrm{d}^2 b} = 2\left(1 - \exp\left[-\frac{\pi^2}{2N_c} r^2 \alpha_s(\mu^2) x g(x, \mu^2 T(b))\right]\right). \quad 18.$$

Here, $T(b)$ is the thickness function—the integrated material encountered by a photon arriving at impact parameter b. The exponential accounts for the probability of the dipole undergoing multiple interactions. For small dipoles, $\mathrm{d}^2\sigma_{q\bar{q}}/\mathrm{d}^2 b \propto r_T^2$.

This dipole formulation has some limitations. It assumes that the dipole does not change as it traverses the target. The lifetime of the fluctuation, $\hbar/M_{q\bar{q}}$, must be longer than the time spent in the nucleus (i.e., $E > \hbar c/R_A$), which is the same condition as in the pQCD formulation, but it is only implicit here. It is usually satisfied at RHIC and the LHC, but it can fail for high-mass final states, in particular at large rapidity for the lower-photon-energy choice in Equation 8.

Because the quark and antiquark momentum fractions are z and $1 - z$, respectively, there is no room for soft gluons; this is necessarily a lowest-order formulation for the photon. However, there is much more freedom in characterizing the target. It is easy to do calculations with colored-glass condensates (CGCs) or other saturation models by altering Equation 18. The presence of significant shadowing leads to a narrowing of the k_T distribution in the interaction, shifting the meson p_T to smaller values (90).

The dipole approach can also accommodate impact parameter–dependent variations in the cross section. It has been used for a large number of different vector meson photoproduction calculations, using different wave functions and dipole-target cross sections. The cross sections often use different models of gluon shadowing and/or saturation, including a different impact parameter dependence. One expects more gluon shadowing in the core of the nucleus (small $\vec{b}_T$) than in its periphery (91).

Figure 5*b* compares ALICE $J/\psi\,\mathrm{d}\sigma/\mathrm{d}y$ lead-target data with predictions from a few representative calculations (92). The impulse approximation treats the nucleus as a collection of independent nucleons, while STARLIGHT uses a Glauber calculation based on parameterized HERA data. BKG-I is a Glauber–Gribov calculation, which uses a gluon density extracted from HERA data (93). Also shown is a leading twist calculation (LTA), while the green line and shaded band show a pQCD calculation where gluon shadowing follows the EPS09 nuclear shadowing parameterization, which is based on non-UPC data. The figure displays three other dipole calculations with different models of the nucleus. The IIM BG curve is based on a CGC model. CGCs are

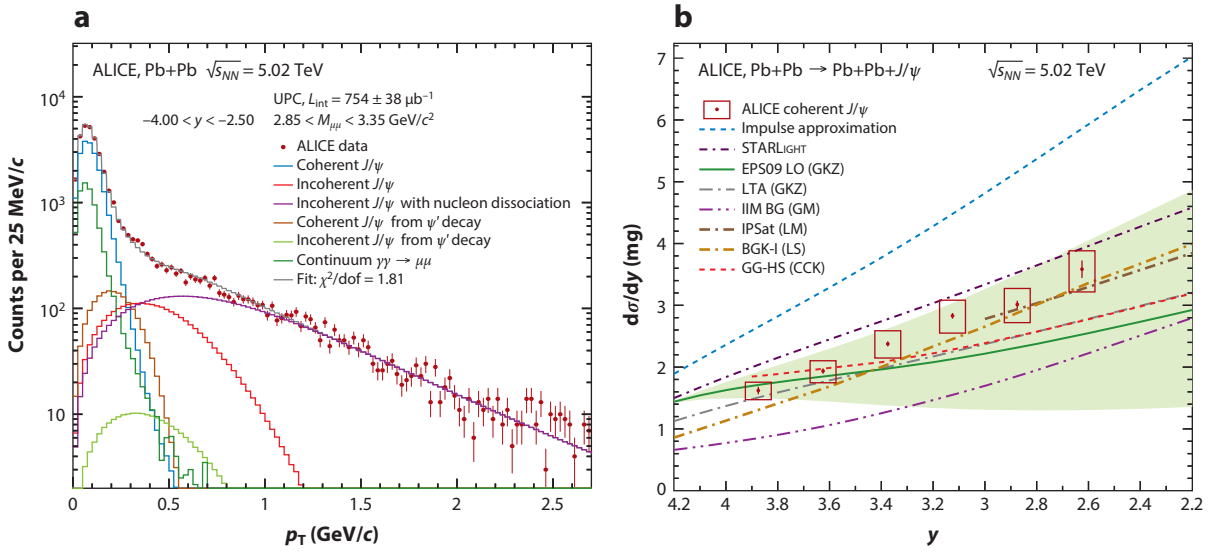

Figure 5

(*a*) Dimuon p_T distribution for dielectron pairs in the J/ψ mass window. (*b*) Differential cross section $d\sigma/dy$ for ultraperipheral collision (UPC) events in 5.02-TeV Pb+Pb data. The theoretical curves in panel *b* show the impulse approximation (*dashed blue line*); a perturbative QCD calculation using the EPS09 nuclear shadowing parameterization (*green line*, with uncertainties shown by the *shaded green band*); a leading twist calculation (LTA, *dashed dotted gray line*); a colored-glass condensate model (IIM BG, *dashed dotted violet line*); the IPSat model, with an impact parameter–dependent dipole-proton cross section (*dashed dotted brown line*); and two Glauber–Gribov calculations without (BKG-I, *dashed dotted tan line*) and with (GG-HS, *dashed red line*) hot spots, as discussed in Section 3.4. Figure adapted from Reference 92 (CC BY 4.0).

a form of saturation model, whereby the nuclei are represented by a classical gluon field. In the IPSat (impact parameter–dependent saturation) model, the dipole-proton cross section depends on the dipole-proton impact parameter; the proton is represented with a Gaussian transverse matter distribution. Finally, the GG-HS model includes gluon hot spots, as discussed below. Aside from the impulse approximation (which, not surprisingly, is far above the data) and the IIM BG calculation (which is considerably below the data), all of the models are in at least marginal agreement with the data. The hot spot and EPS09 calculations are in broad agreement with the data at large rapidity (corresponding mostly to lower photon energies) but diverge for more central rapidities. **Figure 4*a*** shows these data, but the only theory comparison is with the LTA, where the agreement is good, which is slightly surprising because **Figure 5*b*** shows that the LTA curve tends to diverge from the data as $|y|$ is reduced. There are many other calculations of this process with different treatments of gluon density in lead.

Overall, most of these models do a reasonable job of matching the data. Looking ahead, it will be desirable to have a more complete set of comparison data, including the J/ψ, ψ', and Υ—all covering a wide range of rapidities—to more broadly test these models.

3.5. Nuclear Imaging

It is possible to do a two-dimensional Fourier transform to go from $d\sigma/dt$ to $F(b)$, the two-dimensional distribution of interaction sites in the target, as is shown in Equation 16. This is the nuclear analog of a generalized parton distribution. The same equation provides a fairly direct way to probe for changes in the nuclear profile, $F(b)$ due to shadowing. For protons, this offers a

way to probe the generalized parton distributions (94). For UPCs, we focus on heavier ions. The transformation is (95):

$$F(b) \propto \int_0^\infty p_T \mathrm{d}p_T J_0(bp_T)\sqrt{\frac{\mathrm{d}\sigma}{\mathrm{d}t}}, \qquad 19.$$

where J_0 is a modified Bessel function.

There are significant difficulties when this transformation is put into practice, in particular for ions. The relationship is exact if the integral is unbounded, and bp_T must cover several cycles of the Bessel function for an accurate transform. However, the coherent cross section drops faster with increasing t than both incoherent production and the background, so the data have a limited maximum useful p_T. A cutoff at finite p_T introduces windowing artifacts in the transform; the data are effectively convolved with a box function (42), so the calculated $F(b)$ includes the box function as well. The equation assumes that p_T is the pomeron transverse momentum, but the measured p_T also includes the photon p_T. For ion targets, $\mathrm{d}\sigma/\mathrm{d}t$ shows diffractive minima [e.g., as shown by STAR data (42) in **Figure 4*b***]. The minima signal a sign change in the photoproduction amplitude. In Equation 19, $\sqrt{\mathrm{d}\sigma/\mathrm{d}t}$ is this amplitude, so it is necessary to flip its sign when crossing each minimum. In UPCs, these minima are smeared out because of the photon p_T, so determining the dip positions is not straightforward. Studies of the dipion mass (a proxy for Q^2) dependence of $F(b)$ in dipion photoproduction show an intriguing trend, but the systematic uncertainties are large (27). Other approaches to measuring the change in shape of $\mathrm{d}\sigma/\mathrm{d}t$ may be more promising.

3.6. Incoherent Photoproduction

While coherent photoproduction probes the average nuclear configuration, incoherent photoproduction is sensitive to fluctuations—both spatial nuclear fluctuations and local fluctuations in the gluon density. This relationship comes from the optical theorem and is usually embodied in the Good–Walker formalism for diffraction (85). In the Good–Walker approach, the total cross section is (46)

$$\frac{\mathrm{d}\sigma_{\mathrm{tot}}}{\mathrm{d}t} = \frac{1}{16\pi}\langle|A_\Omega|^2\rangle, \qquad 20.$$

where the added Ω subscript on A from Equation 16 explicitly shows that it depends on the target nuclear configuration Ω. In coherent scattering, the initial and final nuclear states are the same, so the amplitudes for the different states are summed and then squared, and

$$\frac{\mathrm{d}\sigma_{\mathrm{coherent}}}{\mathrm{d}t} = \frac{1}{16\pi}|\langle A_\Omega\rangle|^2. \qquad 21.$$

Because the averaging occurs before squaring, coherent photoproduction is sensitive to the average of the configurations. The incoherent cross section is the remainder after the coherent cross section is subtracted from the total:

$$\frac{\mathrm{d}\sigma_{\mathrm{incoherent}}}{\mathrm{d}t} = \frac{1}{16\pi}\left(\langle|A_\Omega|^2\rangle - |\langle A_\Omega\rangle|^2\right). \qquad 22.$$

Through the first term, the incoherent cross section is sensitive to event-by-event fluctuations in the target configuration (96). It requires that the target have an internal structure; without internal structure, there are no inelastic interactions.

One consequence of the Good–Walker approach is that, at very high energies, incoherent photoproduction should disappear. The photonuclear cross section rises with photon energy as photoproduction occurs on gluons with smaller and smaller x values. When the photonuclear cross

section is large enough, the nucleus looks like a black disk. At that point, the internal structure disappears, and the incoherent cross section vanishes (97).

Theorists have used incoherent HERA data on J/ψ photoproduction to study proton shape fluctuations. One analysis (89) found that the cross section for incoherent photoproduction was above the expectations for a smooth proton but was consistent with a model in which the proton contained regions of high gluon density (hot spots). The number of hot spots should increase with photon energy as the target gradually becomes opaque. In one calculation, the incoherent J/ψ photoproduction cross section increases with energy, reaching a maximum at $W_{\gamma p} = 500$ GeV, and then decreases with further increases in $W_{\gamma p}$ (98), within the reach of LHC data. The same calculation shows that the energy at which the incoherent maximum appears increases with vector meson mass, so it is only about $W_{\gamma p} = 20$ GeV for the ρ.

Similar approaches can be applied to nuclei (99). The hot spots are the same as in protons, and the number of hot spots in a nucleus is A times larger than in a proton. Although the differences in inelastic cross sections between the two models are smaller than for proton targets, the hot spot model predicts a larger inelastic J/ψ production, with the difference rising with increasing t. Because saturation sets in at much lower $W_{\gamma p}$ for the ρ, the incoherent ρ photoproduction cross section is predicted to be a small fraction (<5%) of the coherent ρ cross section. That prediction is in some tension with STAR data, where the ratios inferred from integrating $\mathrm{d}\sigma/\mathrm{d}t = A\exp(-bt)$ from References 79 and 100 seem to be considerably higher.

Experimentally, the distinction between coherent and incoherent is not completely straightforward for nuclei. The STAR data in **Figure 4*b*** are actually from the reaction $AA \to A^*A^*\rho^0$; the STAR trigger required neutron emission from each nucleus. In principle, the Good–Walker requirement for coherent photoproduction—that the initial and final states be the same—is not satisfied. However, the data show a clear coherence peak for $p_T < \hbar/R_A$ and at least one diffractive minimum. These observations may be explained using Equation 16, in which coherence depends only on the transverse position of the nucleons. Nuclear excitation is a relatively soft process, and the time scales for it to affect the target nucleus are much longer than the time scales required to produce the vector meson. If the excitation is caused by an additional photon, then it does not destroy the coherence of the vector meson photoproduction. The process essentially factorizes (28, 29). The STAR and ALICE ρ cross section measurements show that this factorization seems to hold quite well (12, 79, 92), except possibly at large p_T.

If the presence or absence of neutrons does not completely determine whether a reaction is coherent or incoherent, the coherent cross section may be found by fitting the incoherent component at large p_T, extrapolating down to small p_T, and subtracting the incoherent cross section from the total, leaving the coherent cross section. The accuracy of this method depends on the functional form that is used. Although an exponential function has frequently been used to model the incoherent $\mathrm{d}\sigma/\mathrm{d}t$, a high-statistics analysis showed that an exponential is not a good fit to the data. A dipole form factor provides a better match (27). Alternatively, the form can be derived from Monte Carlo simulations (92) that include the photon p_T.

A recent ALICE study (92) went farther and divided the incoherent interactions into two classes. In the first, the nucleus dissociated, but the individual nucleons remained intact. In the second, the individual nucleons were excited into higher states. For the first class, the collaboration used a p_T template from the STARLIGHT Monte Carlo (13). For the second, they used a parameterization obtained by HERA studies of the same type of reaction. As **Figure 5*a*** shows, this combination provides a very good fit to the measured J/ψ p_T spectrum.

Even without a trigger that requires neutrons, separating coherent and incoherent interactions is not simple, especially for heavy ions. Because $Z\alpha \approx 0.6$, additional photons may be exchanged, exciting one of the nuclei. It is impossible to tell whether one photon incoherently produced a

vector meson or one photon coherently produced that meson and a second photon dissociated the nucleus.

3.7. Prospects for Measuring Generalized Parton Distributions with Collisions Involving Polarized Protons

Because it can accelerate polarized protons, RHIC can uniquely study polarized generalized parton distributions (GPDs), which describe where the partons are within a nucleon (i.e., as a function of b—similar to Equation 19 but for protons). Polarized GPDs are sensitive to parton polarization (101). The primary experimental observable is the single-spin asymmetry (102), which is proportional to the GPD E^g, which quantifies the gluon orbital momentum. The STAR Collaboration performed an initial measurement of this observable, albeit with a large statistical uncertainty (103). They used pA collisions in which photons from the gold nucleus illuminated the polarized proton target. The proposed AFTER experiment plans to study this process with unpolarized lead ions striking a polarized proton target (102). Proposals have also been made to use time-like Compton scattering at the LHC to probe other GPDs, primarily for quarks (104).

3.8. Photoproduction of Exotic Hadrons

Reggeon exchange allows a wide range of final states since spin and charge can be exchanged. Because the spin or charge exchange alters the target, coherence is unlikely to be maintained, so most studies of reggeon exchange have considered proton targets. Reggeon exchange rates are high. The predicted photoproduction rate for the $a_2^+(1320)$, a "standard candle" $q\bar{q}$ meson, is about a billion mesons per year at both RHIC and the LHC (105). Thus, states with small couplings to photons can be observed. The cross sections peak at low (a few times threshold) photon energies. These low photon energies correspond to large-rapidity final states. A given final state will be nearer midrapidity at RHIC than at the LHC. Measurements at RHIC will provide good opportunities to study exotic hadrons (105), especially with future forward upgrades such as the STAR Forward Tracking and Calorimeter Systems (106).

UPC photoproduction is a way to study the exotic XYZ states (107). These states are heavy, containing a $c\bar{c}$ pair, so they are mostly beyond the reach of fixed-target photoproduction. Photoproduction data would help elucidate the nature of these states (108–110). Pentaquarks may also be produced, via $\gamma p \rightarrow P$ (111). Jefferson Lab's GlueX experiment has recently put strong limits on photoproduction of $c\bar{c}$-containing pentaquarks (112). UPCs should be useful in the study of heavier pentaquarks, such as those that contain $b\bar{b}$ pairs.

3.9. Photoproduction in Peripheral Hadronic Collisions

Although the criterion $b > 2R_A$ affects its visibility (and provides the largest rate, via Z^4), photoproduction still occurs when $b < 2R_A$. Both STAR (113) and ALICE (114) have observed an excess, over hadronic expectations, of J/ψ with $p_T < 150$ MeV/c in peripheral collisions. The cross section for these J/ψ generally agrees with photoproduction calculations (30, 115, 116). These calculations raise an interesting question: Do nucleons that interact hadronically also contribute to the photoproduction amplitude? If they lose energy, the photoproduction cross section will be drastically reduced. The hadronic interactions affect both the p_T distribution of the J/ψ and their abundance. The J/ψ survival probability also merits study. A J/ψ produced inside the hadronic fireball may be dissociated before it can decay. Even if it is produced outside the fireball, with its low transverse velocity and long lifetime (compared with the fireball), it may be engulfed

before it decays. High-statistics studies of how the cross section depends on b could shed light on these questions.

Photoproduced J/ψ can also aid our understanding of the hadronic collision by providing an independent (from the hadronic interaction) measurement of the reaction plane. Two factors have some sensitivity to the reaction plane. The first factor is Equation 9, which relates the J/ψ p_T spectrum to the angle between the J/ψ p_T and $\vec{b}$. The second factor, the J/ψ polarization, provides additional information since the J/ψ linear polarization follows the photon polarization, which follows its $\vec{E}$ field, which is correlated with $\vec{b}$. This polarization may be observed in the azimuthal angle of the decay lepton p_T. The J/ψ transverse momenta tend to follow their polarization (28). These handles depend on the direction of $\vec{b}$ and, from that, the reaction plane.

4. TWO-PHOTON INTERACTIONS

The large photon fluxes from each nucleus, which each scales as Z^2, provide a high rate of photon–photon collisions with photon energies spanning a wide kinematic range—in particular at the LHC, where the Lorentz factor is quite large. Photon interactions lead to a wide variety of final states. They couple to all charged particles, including leptons, quarks, and charged gauge bosons (2, 117). They also couple to neutral final states through loop diagrams and thus offer the possibility of observing direct production of Higgs bosons as well as two-photon final states [now also known as light-by-light scattering (118)].

4.1. Two-Photon Luminosity

The production rates for exclusive particle production from two-photon collisions can be factorized into a two-photon "luminosity" (or flux) and the cross section [$\sigma(\gamma\gamma \to X)$] (119, 120). The ultraperipheral two-photon flux (often referred to as the two-photon luminosity) is typically calculated by integrating over the two separate fluxes, with the requirements that (*a*) the nuclei do not overlap, using $P_{0\text{had}}$; (*b*) the production does not take place inside either nucleus; and (*c*) a specific number of neutrons is emitted in each direction (or this requirement can be ignored for an inclusive selection) (13, 121):

$$\frac{\mathrm{d}^2N}{\mathrm{d}k_1\mathrm{d}k_2} = \int_{b_1>R_A} \mathrm{d}^2\vec{b}_1 \int_{b_2>R_A} \mathrm{d}^2\vec{b}_2 N(k_1,b_1)N(k_2,b_2)P_{0\text{had}}(|\vec{b}_1-\vec{b}_2|)P_{\text{fn}}(|\vec{b}_1-\vec{b}_2|). \qquad 23.$$

This integral can be simplified by changing variables, to integrate over the absolute values of b_1 and b_2 and the angle between them (10, 122). This approach is used in most calculations. The second assumption, that there is no production inside either nucleus, is perhaps too strong, although the contributions to the flux should be limited because of the rapid falloff of the field strengths inside a nucleus.

4.2. Dilepton Production: $\gamma\gamma \to \ell\ell$

Most existing measurements of $\gamma\gamma$ processes in heavy-ion collisions involve leptonic final states $\gamma\gamma \to \ell^+\ell^-$. At lower pair masses ($M < 10$ GeV), they are typically performed in tandem with the vector meson measurements described above (123, 124). The exclusive final state is particularly simple, consisting primarily of two back-to-back charged particles with opposite signs, and many high-energy and nuclear physics experiments have been designed with capabilities including excellent lepton identification and precise momentum measurements. STAR has performed a series of electron pair measurements using their large acceptance time projection chamber (TPC),

initially triggered by a mutual Coulomb exchange (neutrons in both ZDCs; see Section 2.2) and confirmed by signals from the TPC and time-of-flight counters, to select events with electron pair candidates (34, 125). ATLAS uses a sophisticated multilevel trigger system to select events with a single muon, vetoing on large transverse energies in the rest of the event, but with no selection on the forward neutron topology (126).

Figure 6 shows dilepton cross sections from STAR (127) (as a function of invariant mass) and ATLAS (126) (as a function of pair rapidity, for three mass ranges) and compared with calculations, including ones from STARLIGHT (13). ATLAS restricts the measurements to relatively large muon transverse momenta ($p_{T\mu} > 4$ GeV in $|\eta| < 2.4$). These requirements also select large mass (ATLAS chose $M_{\mu\mu} > 10$ GeV), but there is no restriction on the forward neutron topology, and thus the full fiducial cross section is measured. STAR measures much softer electrons ($p_{Te} > 0.2$ GeV in $\eta < 1$) and thus much lower masses, but its UPC pairs are required to have forward neutrons in both ZDCs, thus limiting the cross section to only a small fraction of the total. STARLIGHT describes the overall magnitude of the dilepton cross section over a wide range of pair mass and rapidity, although it is found to underpredict the ATLAS data in the forward region, and STAR sees the possibility of some overall underprediction of the data.

Although generalized EPA and full QED calculations (33) describe the magnitude of the cross section better than STARLIGHT does, STAR reports that all calculations have been found to be consistent with the data within the stated overall scale uncertainties of 13%. The STAR data are for e^+e^-; here, the Weizsäcker–Williams approach may be more questionable than for heavier leptons because, uniquely, $m_e < \hbar/R_A$. Other groups (128–131) have performed calculations of the exclusive dilepton cross sections, albeit with somewhat different assumptions regarding the impact parameter dependence of the absorptive corrections, or by explicit inclusion of the nuclear form factors. The details of these features can have observable consequences for the magnitude of the cross section. In particular, the detailed shape of the pair spectrum at large values of the pair invariant mass and pair rapidity distributions is sensitive to the higher-energy photons in the initial state. Allowing pair production within the two nuclei improves agreement with the STAR data (132) and could improve agreement with the ATLAS data. STAR has also observed angular modulations of the pair momentum relative to the single-electron momenta, reflecting the linear polarization of the initial photons (127, 133).

Tau (τ) leptons can be pair-produced only for incoming diphoton invariant masses above 3.5 GeV, so they are difficult to produce at RHIC. However, they have been observed to exist at the LHC through leptonic decays in which one decays to an electron and the other to a muon (134), and they should also be observable as low-activity events containing one lepton and one or three charged tracks. The coupling between the τ and photon is sensitive to a combination of modifications of $a_\tau = (g_\tau - 2)/2$ [e.g., due to lepton compositeness (135) or coupling to supersymmetric particles (136)] as well as to an electric dipole moment of the τ itself. These modifications are predicted to have an observable effect on the p_T of the decay leptons and hadrons, with a systematic hardening of the spectrum correlating with changes in a_τ or the τ electric dipole moment d_τ (137, 138).

4.3. Dilepton p_T and Impact Parameter Selections

As has been emphasized throughout this review, and in particular in Section 2.3, one key feature that distinguishes production processes in purely electromagnetic processes from heavy-ion collisions is the very low p_T of the initial-state photons. In dilepton processes, this leads to final-state pair p_T values of ~20–30 MeV. The pair p_T can be measured accurately for low-p_T leptons (e.g., in STAR) but can only be estimated through the dilepton opening angle for high-p_T leptons (e.g., the

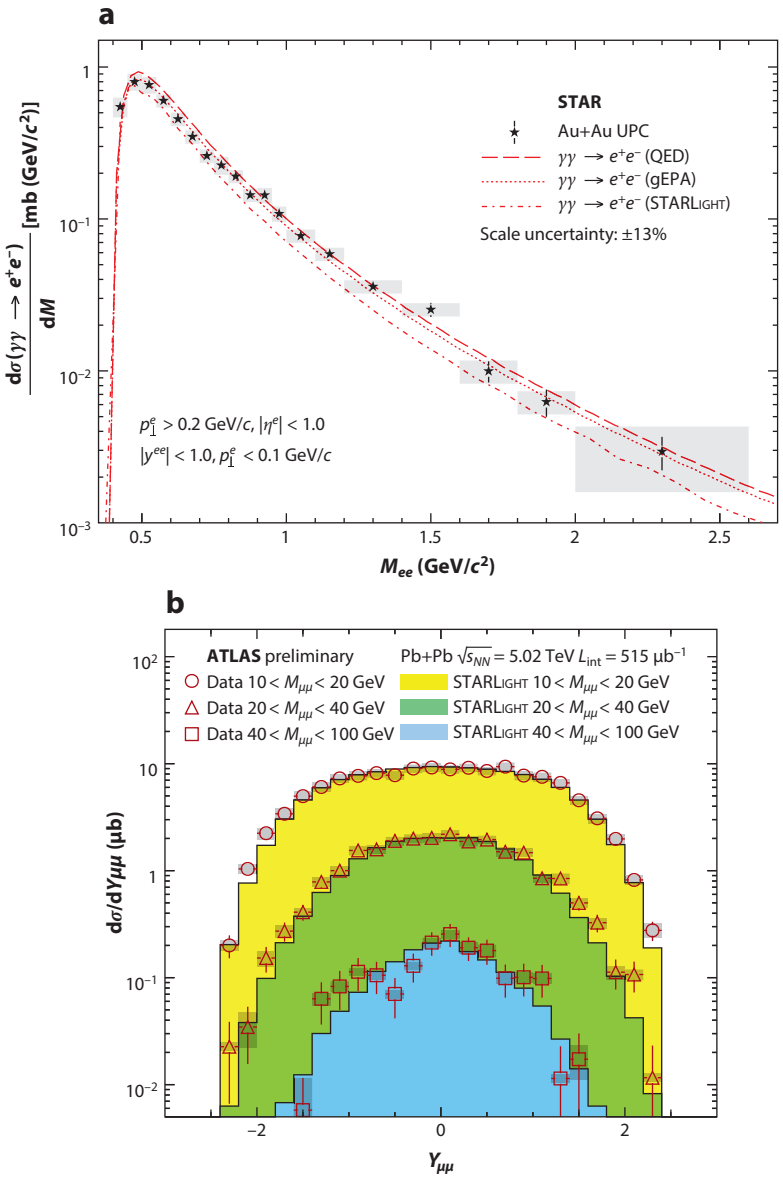

Figure 6

(*a*) Distribution of dielectron invariant mass from STAR (127) compared with three calculations using QED including a generalized EPA calculation from Zha et al. (132) and STARLIGHT. Panel adapted from Reference 127. (*b*) Distribution of dimuon rapidity, in invariant mass selections, from ATLAS compared with STARLIGHT calculations. Panel adapted from Reference 126 (CC BY 4.0).

acoplanarity, $\alpha = 1 - |\Delta\phi|/\pi$), as measured in ATLAS. The detailed shapes of these distributions are sensitive to several different aspects of the underlying physics.

Large values of pair p_T or α are generally inaccessible in most calculations, which typically provide the intrinsic p_T via the nuclear form factor. This part of the dilepton angular spectrum

is generally sensitive to final-state higher-order photon emissions, as shown diagrammatically in **Figure 1*f***. These contributions have generally not been included in existing event generators, although References 139 and 140 have demonstrated analytically, using a Sudakov formalism, that they are already consistent with the preliminary ATLAS data. Similar success modeling the experimental data should be possible using the final-state QED parton showering already available in Pythia 8 (141). Pythia also incorporates nuclear photon fluxes (15), albeit without overlap removal.

By contrast, pairs with small pair p_T or α have been found to be particularly sensitive to quantum interference effects related to constraints on the impact parameter between the two colliding nuclei. Up to this point, all processes have been assumed to exclude the fraction of the cross section where the nuclei overlap as well as instances in which the production vertex is inside either nucleus (121). This choice is made both out of convenience and to alleviate potential conceptual issues. Distinguishing signal processes from backgrounds is generally more difficult in events in which hadronic processes also occur. There are also open questions as to where a coherent process can take place in proximity to more violent hadronic collisions. A subtler issue arises from the limits of the equivalent photon approximation. In comparisons of typical EPA calculations with those that use a more complete QED formalism, replacing the photon probability densities with QED amplitudes based on point charge nuclei convolved with measured form factors, these integrals involve a phase $i\vec{b}\cdot\vec{q}$, where $\vec{q}$ is the vector pair transverse momentum (31–33). Restricting the impact parameter close to zero can lead to large oscillations that tend to deplete the cross sections for low pair p_T and lead to increased broadening in the final p_T or α distributions. This effect was first observed in dielectron data from STAR (125), by comparison with QED calculations from Hencken et al. (142) that evinced a clear suppression at low pair p_T relative to EPA calculations.

More recently, STAR studied data from Au+Au and U+U collisions measured with a UPC selection, and for very peripheral (60–80%) hadronic interactions (34, 127). A distinct broadening of the p_T distributions was observed (see **Figure 7*a***)—an effect that had been postulated as evidence for trapped magnetic fields but that was revised based on the existence of updated calculations in Reference 33. Similarly, ATLAS observed nearly back-to-back muon pairs in hadronic Pb+Pb

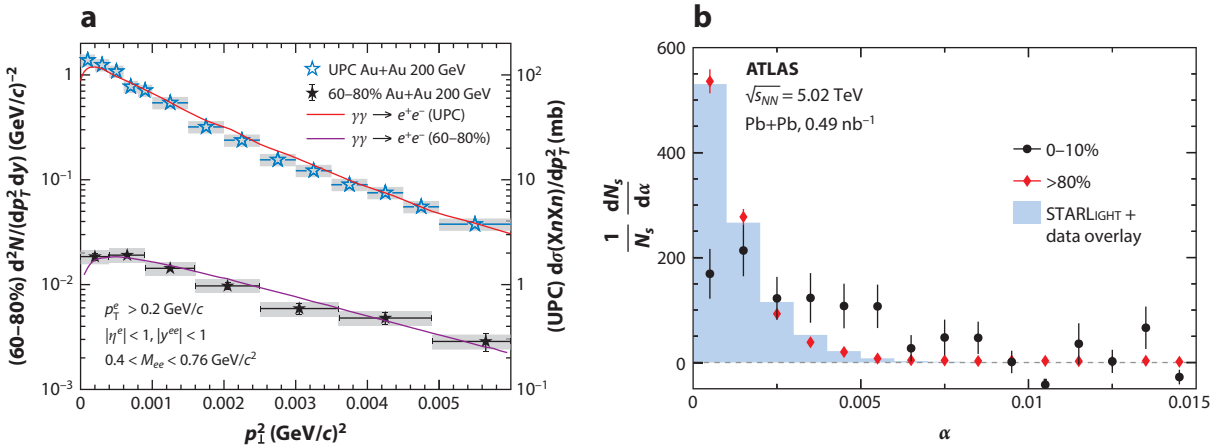

Figure 7

(*a*) STAR data on dielectron p_T distributions in ultraperipheral and peripheral Au+Au collisions (127) compared with QED calculations from Zha et al. (132). Panel adapted from Reference 127. (*b*) ATLAS comparisons of dimuon acoplanarity (α) between ultraperipheral and central collisions, showing a significant broadening of the dimuon opening angle. Panel adapted from Reference 35 (CC BY 4.0).

collisions at the LHC, but over the full (0–100%) centrality range. A clear centrality-dependent broadening of the α relative to a UPC-like selection was observed (35), as shown in **Figure 7*b***. This finding was interpreted by the ATLAS Collaboration and other authors as a possible probe of the charged constituents of the hot, dense quark gluon plasma. However, a preliminary update of this measurement with more than three times the integrated luminosity (36) observed that the acoplanarity distributions were not just broadened in more central collisions but in fact peaked at nonzero values. Intriguingly, the QED calculations in Reference 33 seem to have predicted the dip at zero and to have quantitatively described a large fraction of the full distribution, suggesting that no exotic QCD physics is needed; rather, what is needed is a more careful treatment of QED interference effects related to constraints on the impact parameter range.

4.4. Bound-Free Pair Production, Antihydrogen Production, and Accelerator Luminosity Limits

Pair production does not always result in a free electron; the electron may be produced bound to one of the incident ions (1). This process is known as bound-free pair production (BFPP). The cross section for BFPP with the electron captured in the *K* shell is (143)

$$\sigma = \frac{33\lambda_c^7 Z_T^5 Z_p^2 \alpha^7}{20(e^{2\pi\alpha Z}-1)}, \left(\ln\frac{\delta\gamma}{2} - \frac{5}{3}\right), \qquad 24.$$

where Z_p and Z_T are the charge of the photon-emitting nucleus and target nucleus, respectively; λ_c is the Compton wavelength; and $\delta \approx 0.681$. The flux scaling with Z_p^2 is standard for photon emission, while Z_T enters at the fifth power because the depth and width of the electric potential well increase rapidly with *Z*. The total BFPP cross section is about 20% larger because of the possibility of capture into higher orbitals. The cross section is maximal for relatively low-energy photons (2.5 MeV in the target rest frame), so the ion momentum is largely unchanged despite the charge change.

The cross section for BFPP is large—about 276 barns for each target beam for lead–lead collisions at the LHC (39). Because the produced single-electron ions have a larger magnetic rigidity, they are lost from the beam. Along with Coulomb excitation of ions, these single-electron ions are a major source of beam and luminosity loss over time.

BFPP at the LHC produces a well-collimated beam of single-electron lead ions, which diverge from the circulating fully stripped lead ions (144–146). The trajectory of this beam depends on the LHC magnet optics, but it will strike the beam pipe around 400 m downstream of each interaction point. This beam carries significant power, which produces local heating that may cause the superconducting magnets to quench. In a controlled test, a magnet quench occurred at a luminosity of 2.3×10^{27} cm^{-2} s^{-1}, which is 2.3 times the design luminosity (146). Although the local heating problem can be alleviated by shifting the losses using orbit bumps to a less problematic region of the collider, BFPP is an important constraint on high-energy accelerator design for heavy ions.

BFPP can also produce antihydrogen: positrons bound to antiprotons. This process was used to produce the first antihydrogen atoms at CERN's Low Energy Antiproton Ring (LEAR) (147) and then at the Fermilab Antiproton Accumulator (148). Detection is easier with low-energy collisions, in which the antihydrogen velocity is relatively modest.

Similar reactions occur with muons (149), taus, and even charged mesons. The cross section for muonic BFPP has been calculated to be 0.16 mb (150); the cross section for heavier particles is smaller (<100 μb). Because these single-lepton atoms have large rapidities, they can only be detected with a far-forward spectrometer.

It is also possible to produce the bound state $\mu^+\mu^-$ (151). These bound states are produced near midrapidity. In lead–lead collisions at the LHC, the cross section is ∼1 μb, so the production rate is large; the difficulty is in detecting the two soft photons in the para-muonium final state.

4.5. Light-by-Light Scattering: $\gamma\gamma \to \gamma\gamma$

Classically, QED obeys the principle of superposition, such that electromagnetic fields are purely additive and photons do not interact with each other. However, the Standard Model predicts (118, 152) that photons can interact via loop diagrams with internal lines containing quarks, leptons, and charged W gauge bosons, as shown in **Figure 1**. The cross section is sensitive to beyond–Standard Model processes such as magnetic monopoles (153), vector fermions (154), and axion-like particles (155, 156). Related processes have been observed by Delbrück scattering off the Coulomb field of a nucleus (157) as well as by photon splitting (158), but the direct process was only recently observed, with greater than 5σ significance, by the ATLAS Collaboration (159) using 1.7 nb^{-1} of Pb+Pb data at 5.02 TeV, after earlier evidence from ATLAS (160) and CMS (161) with only 0.4–0.5 nb^{-1}.

ATLAS (159) used photons measured in their electromagnetic calorimeters, rejecting backgrounds by requiring no tracks in the tracking detectors matched to the photon. The primary fiducial selection is to have each photon with $E_T > 3$ GeV and a maximum $|\eta| < 2.4$, approximating the acceptance of the electromagnetic calorimeter, and an invariant mass above 6 GeV. Before the correction factor is applied, backgrounds are removed by data-driven techniques to estimate the probability of mis-tagging electrons as photons and also by a data-driven normalization of diphoton events produced through central exclusive production in a two-gluon exchange. After all selections, 59 events were found in the signal regions, where 12 ± 3 background events were expected. The significance of this result relative to a background-only hypothesis was evaluated for $A_\phi < 0.005$ with 42 signal-region events, and 6 ± 2 background events are expected, giving a significance of 8.2σ.

The CMS result (161) used similar techniques and addressed the same background contributions but with a slightly larger fiducial space ($E_T > 2$ GeV per photon, and $M_{\gamma\gamma} > 5$ GeV). The lower integrated luminosity provided only 14 events in the signal region with approximately 4 ± 1 background events expected, giving a significance of 3.7 standard deviations. CMS also provided upper limits on the axion-like particle production cross section, $\gamma\gamma \to a \to \gamma\gamma$, over a range of $5 < m_a < 90$ GeV, and translated the results to limits on the photon–axion coupling $g_{a\gamma}$. These limits are extracted based on two assumptions (155); the first assumption is photon-only coupling (shown in **Figure 8*b***), where new limits are provided over $5 < m_a < 50$ GeV, and the second assumption is hypercharge coupling (not shown), where new limits are set only in a more limited range $5 < m_a < 10$ GeV, just beyond the region explored by an earlier ATLAS 3γ analysis (162).

4.6. Hadron Production: $\gamma\gamma \to X$

Many early papers discussed two-photon production of mesons and meson pairs. Unfortunately, however, the cross sections and production rates are rather small (3), and even the benchmark $\gamma\gamma \to f_2(1270)$ process has not yet been observed. In many cases, the calculated production rates due to feed-down from photoproduction are larger than the two-photon production rates. For example, the rate for coherent photoproduction of the J/ψ followed by $J/\psi \to \eta_c\gamma$ is considerably larger than for $\gamma\gamma \to \eta_c$ (163). The photon is too soft to be seen in collider detectors, and the two processes have very similar η_c kinematics.

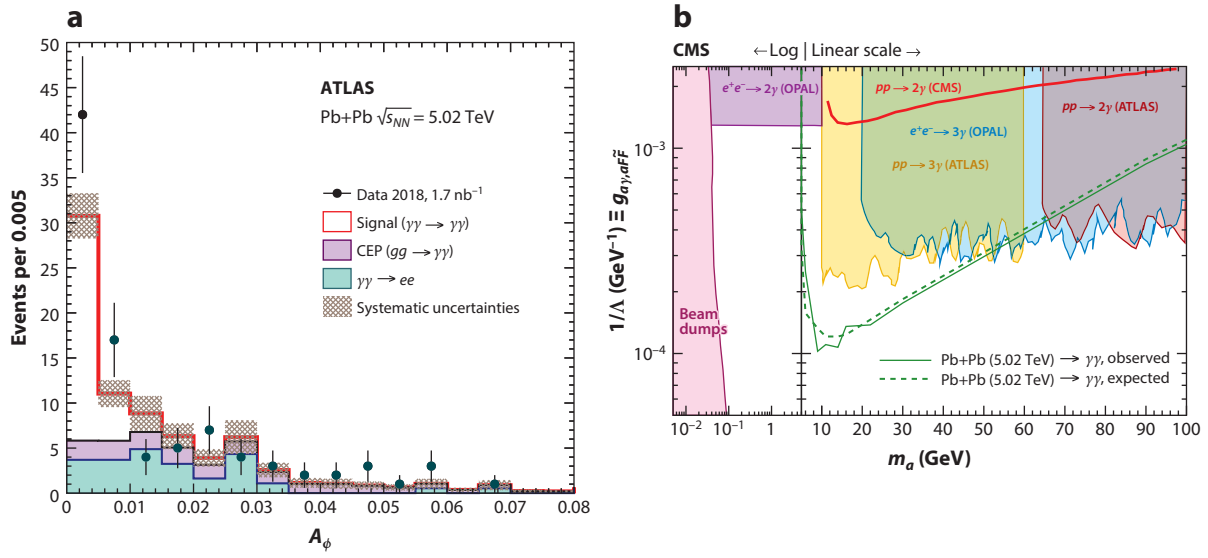

Figure 8

(*a*) Acoplanarity (A_ϕ) distributions from ATLAS exclusive diphoton events compared with expectations from the two primary backgrounds [e^+e^- and central exclusive production (CEP)]. Panel adapted from Reference 159 (CC BY 4.0). (*b*) Upper limits set on axion-like particle production, assuming only coupling to photons. Panel adapted from Reference 161 (CC BY 4.0).

5. FUTURE PROSPECTS

The current heavy-ion data sets (*AA* and *pA*) have not been fully utilized to explore all possible aspects of the physics discussed in this review. One can expect further improvements for processes that involve higher photon energies using the full integrated luminosity in the LHC Run 2 data set (up to about 2 nb^{-1}). However, LHC Runs 3 and 4, while keeping the same beam energies (or perhaps increasing by 7.6%), will collect nearly an order of magnitude more integrated luminosity for both ion–ion and proton–ion collisions (17). A run with intermediate-mass ions is also possible and would allow higher UPC luminosity due to the substantially reduced BFPP and Coulomb excitation cross sections.

CERN's planned Future Circular Collider and the proposed Chinese SPPC (7) should allow for a greatly expanded scope of measurements. They will have a higher beam energy by nearly an order of magnitude, which should enable studies of photoproduction of top quarks, photoproduction and two-photon physics studies of vector bosons, and improved opportunities to search for physics beyond the Standard Model.

The next generation of RHIC experiments, with an updated STAR detector and sPHENIX—a newly built collider experiment focusing on extremely high data rates—will have access to enhanced statistics on exclusive dilepton, vector meson, and possibly even UPC jet physics. With the new generation of high-precision vertex detectors, studies of photoproduction of open charm should also be possible.

UPC photoproduction studies will be complemented by photoproduction ($Q^2 \approx 0$) and electroproduction ($Q^2 > 0$) studied at a future electron–ion collider, such as the planned EIC at Brookhaven National Laboratory (101) and CERN's LHeC (20). Although, as shown in **Table 1**, most of the electron–ion collider designs reach lower $W_{\gamma p}$ than the LHC does, they offer considerably higher luminosity. More importantly, electrons can radiate photons over a wide

range of Q^2, and this Q^2 can be determined from observing the scattered electron no matter what reaction occurs. The wide Q^2 range corresponds to a broad size distribution of dipoles regardless of reaction type. This wider range will allow us to better probe the gluon distribution in nuclei on different length scales. An electron–ion collider will also allow us to study two-photon physics where one of the photons is highly virtual.

SUMMARY POINTS

1. Ultraperipheral collisions are the energy frontier for photonuclear and two-photon physics, with the LHC reaching higher center-of-mass energies than any existing alternative.
2. High-precision J/ψ photoproduction data are consistent with moderate shadowing scenarios.
3. Two-photon processes that involve dilepton and two-photon final states are providing new insights from quantum electrodynamics and potential access to physics beyond the Standard Model.

FUTURE ISSUES

1. Existing and future RHIC and LHC data can be probed to study a wide range of photoproduction and two-photon reactions, in particular through studies of a wider range of final-state mesons, all species of dileptons, and heavy quarks.
2. Precision studies of benchmark photoproduction of multiple heavy mesons, with and without forward neutron topological selections, will be needed to improve our knowledge of nuclear structure, to test different saturation and colored-glass condensate models, and to measure nuclear shadowing.
3. A future high-energy FCC-hh collider will extend photoproduction and two-photon physics studies by a factor of seven in energy, opening the door to study top quark physics, probe parton distributions down to $x \approx 10^{-7}$, observe $\gamma\gamma \to H$, and provide complementary probes to physics beyond the Standard Model.
4. A future electron–ion collider will be able to make high-precision complementary studies of many photoproduction channels over a wide range of Q^2.

DISCLOSURE STATEMENT

The authors are not aware of any affiliations, memberships, funding, or financial holdings that might be perceived as affecting the objectivity of this review.

ACKNOWLEDGMENTS

The authors thank their STAR, ALICE, and ATLAS colleagues. This work was supported by the US Department of Energy, Office of Science, Office of Nuclear Physics, under contract numbers DE-AC02-05CH11231 and DE-SC0012704.

LITERATURE CITED

1. Bertulani CA, Baur G. *Phys. Rep.* 163:299 (1988)
2. Baur G, et al. *Phys. Rep.* 364:359 (2002)
3. Bertulani CA, Klein SR, Nystrand J. *Annu. Rev. Nucl. Part. Sci.* 55:271 (2005)
4. Baltz AJ, et al. *Phys. Rep.* 458:1 (2008)
5. Contreras JG, Tapia Takaki JD. *Int. J. Mod. Phys. A* 30:1542012 (2015)
6. Klein S, Nystrand J. *Phys. Today* 70:40 (2017)
7. Ahmad M, et al. (CEPC-SPPC Study Group) *CEPC-SPPC preliminary conceptual design report*. Rep. IHEP-CEPC-DR-2015-01/IHEP-EP-2015-01/IHEP-TH-2015-01, Inst. High Energy Phys., Chin. Acad. Sci., Beijing (2015)
8. Massacrier L, Lansberg JP, Szymanowski L, Wagner J. Quarkonium-photoproduction prospects at a fixed-target experiment at the LHC (AFTER@LHC). In *Proceedings of the PHOTON-2017 Conference*, ed. D d'Enterria, A de Roeck, M Mangano, pp. 163–68. Geneva: CERN. **http://cds.cern.ch/record/2666846/files/fulltext1625748.pdf** (2018)
9. Papageorgiu E. *Phys. Rev. D* 40:92 (1989)
10. Cahn RN, Jackson JD. *Phys. Rev. D* 42:3690 (1990)
11. Klein S, Nystrand J. *Phys. Rev. C* 60:014903 (1999)
12. Adler C, et al. (STAR Collab.) *Phys. Rev. Lett.* 89:272302 (2002)
13. Klein SR, et al. *Comput. Phys. Commun.* 212:258 (2017)
14. Harland-Lang LA, Khoze VA, Ryskin MG. *Eur. Phys. J. C* 79:39 (2019)
15. Helenius I. *Proc. Sci.* HardProbes2018:118 (2018)
16. Harrison S, Ludlam T, Ozaki S. *Nucl. Instrum. Meth. A* 499:235 (2003)
17. Citron Z, et al. Report from Working Group 5: future physics opportunities for high-density QCD at the LHC with heavy-ion and proton beams. In *Physics at the HL-LHC, and Perspectives at the HE-LHC*, ed. A Dainese, et al., pp. 1159–410. Geneva: CERN. **https://e-publishing.cern.ch/index.php/CYRM/article/view/955/772** (2019)
18. Abada A, et al. *Eur. Phys. J. ST* 228:755 (2019)
19. Montag C, et al. eRHIC electron ring design status. In *Proceedings of the 10th International Particle Accelerator Conference (IPAC2019)*, ed. M Boland, H Tanaka, D Button, pp. 794–96. Geneva: JACoW. **http://accelconf.web.cern.ch/ipac2019/papers/moprb093.pdf** (2019)
20. Abelleira Fernandez JL, et al. *J. Phys. G* 39:075001 (2012)
21. Klein SR, Nystrand J. *Phys. Rev. Lett.* 92:142003 (2004)
22. Fermi E. *Z. Phys.* 29:315 (1924)
23. von Weizsäcker CF. *Z. Phys.* 88:612 (1934)
24. Williams EJ. *Kong. Dan. Vid. Sel. Mat. Fys. Med.* 13N4:1 (1935)
25. Miller ML, Reygers K, Sanders SJ, Steinberg P. *Annu. Rev. Nucl. Part. Sci.* 57:205 (2007)
26. Drees M, Zeppenfeld D. *Phys. Rev. D* 39:2536 (1989)
27. Klein SR. *Proc. Sci.* DIS2018:047 (2018)
28. Baur G, et al. *Nucl. Phys. A* 729:787 (2003)
29. Baltz AJ, Klein SR, Nystrand J. *Phys. Rev. Lett.* 89:012301 (2002)
30. Zha W, et al. *Phys. Rev. C* 97:044910 (2018)
31. Vidovic M, Greiner M, Best C, Soff G. *Phys. Rev. C* 47:2308 (1993)
32. Vidovic M, Greiner M, Soff G. *Phys. Rev. C* 48:2011 (1993)
33. Zha W, Brandenburg JD, Tang Z, Xu Z. arXiv:1812.02820 [nucl-th] (2018)
34. Adam J, et al. (STAR Collab.) *Phys. Rev. Lett.* 121:132301 (2018)
35. Aaboud M, et al. *Phys. Rev. Lett.* 121:212301 (2018)
36. ATLAS Collab. *Measurement of non-exclusive dimuon pairs produced via $\gamma\gamma$ scattering in Pb+Pb collisions at $\sqrt{s_{NN}} = 5.02$ TeV with the ATLAS detector*. Tech. Rep. ATLAS-CONF-2019-051, CERN, Geneva (2019)
37. Nystrand J, Klein S. (STAR Collab.) arXiv:nucl-ex/9811007 (1998)
38. Berman BL, Fultz SC. *Rev. Mod. Phys.* 47:713 (1975)
39. Baltz AJ, Rhoades-Brown MJ, Weneser J. *Phys. Rev. E* 54:4233 (1996)
40. Pshenichnov IA, et al. *Phys. Rev. C* 64:024903 (2001)

41. Baltz AJ, Chasman C, White SN. *Nucl. Instrum. Meth. A* 417:1 (1998)
42. Adamczyk L, et al. (STAR Collab.) *Phys. Rev. C* 96:054904 (2017)
43. Chiu M, et al. *Phys. Rev. Lett.* 89:012302 (2002)
44. Abelev B, et al. *Phys. Rev. Lett.* 109:252302 (2012)
45. Broz M, Contreras JG, Tapia Takaki JD. arXiv:1908.08263 [nucl-th] (2019)
46. Klein SR, Mantysaari H. *Nat. Rev. Phys.* 1:662 (2019)
46a. ATLAS Collab. Performance plots for pp and Pb+Pb collisions at $\sqrt{s_{NN}} = 5.02$ TeV. *AtlasPublic Web*. **https://atlas.web.cern.ch/Atlas/GROUPS/PHYSICS/PLOTS/HION-2015-001/** (2015)
47. ATLAS Collab. *Photo-nuclear dijet production in ultra-peripheral Pb+Pb collisions*. Tech. Rep. ATLAS-CONF-2017-011, CERN, Geneva (2017)
48. Adeluyi A, Bertulani CA. *Phys. Rev. C* 85:044904 (2012)
49. Klein SR, Nystrand J, Vogt R. *Phys. Rev. C* 66:044906 (2002)
50. Gonçalves VP, Sampaio dos Santos G, Sena CR. *Nucl. Phys. A* 976:33 (2018)
51. Strikman M, Vogt R, White SN. *Phys. Rev. Lett.* 96:082001 (2006)
52. Klein SR, Nystrand J, Vogt R. *Eur. Phys. J. C* 21:563 (2001)
53. Gonçalves VP. *Phys. Rev. D* 88:054025 (2013)
54. ATLAS Collab. *Two-particle azimuthal correlations in photo-nuclear ultra-peripheral Pb+Pb collisions at 5.02 TeV with ATLAS*. ATLAS Note ATLAS-CONF-2019-022, CERN, Geneva (2019)
55. Forshaw JR, Ross DA. *Quantum Chromodynamics and the Pomeron*. Cambridge, UK: Cambridge Univ. Press (1997)
56. Sirunyan AM, et al. *Eur. Phys. J. C* 79:277 (2019)
57. Sirunyan AM, et al. *Eur. Phys. J. C* 79:702 (2019)
58. Acharya S, et al. *Eur. Phys. J. C* 79:402 (2019)
59. LHCb Collab. *Central exclusive production of* J/ψ *and* $\psi(2S)$ *mesons in pp collisions at* $\sqrt{s} = 13$ *TeV*. LHCb Note LHCb-CONF-2016-007/CERN-LHCb-CONF-2016-007, CERN, Geneva (2016)
60. Contreras JG. *Phys. Rev. C* 96:015203 (2017)
61. Klein SR, Nystrand J. *Phys. Rev. Lett.* 84:2330 (2000)
62. Abelev BI, et al. *Phys. Rev. Lett.* 102:112301 (2009)
63. Klein SR, Nystrand J. *Phys. Lett. A* 308:323 (2003)
64. Bauer TH, Spital RD, Yennie DR, Pipkin FM. *Rev. Mod. Phys.* 50:261 (1978). Erratum: *Rev. Mod. Phys.* 51:407 (1979)
65. Abramowicz H, Caldwell A. *Rev. Mod. Phys.* 71:1275 (1999)
66. Jones SP, Martin AD, Ryskin MG, Teubner T. *J. High Energy Phys.* 1311:85 (2013)
67. Collins JC, Frankfurt L, Strikman M. *Phys. Lett. B* 307:161 (1993)
68. Klein SR. *Nucl. Phys. A* 967:249 (2017)
69. Shuvaev AG, Golec-Biernat KJ, Martin AD, Ryskin MG. *Phys. Rev. D* 60:014015 (1999)
70. Flett CA, et al. arXiv:1912.09128 [hep-ph] (2019)
71. Jones SP, Martin AD, Ryskin MG, Teubner T. *Eur. Phys. J. C* 76:633 (2016)
72. Flett CA, et al. *Phys. Rev. D* 101:094011 (2020)
73. Adam J. *Proc. Sci.* DIS2016:187 (2016)
74. McNulty R. *Proc. Sci.* DIS2016:181 (2016)
75. Frankfurt L, Strikman M, Zhalov M. *Phys. Rev. C* 67:034901 (2003)
76. Khachatryan V, et al. *Phys. Lett. B* 772:489 (2017)
77. Guzey V, Zhalov M. *J. High Energy Phys.* 1310:207 (2013)
78. Frankfurt L, Guzey V, Strikman M. *Phys. Rep.* 512:255 (2012)
79. Abelev BI, et al. *Phys. Rev. C* 77:034910 (2008)
80. Adam J, et al. *J. High Energy Phys.* 1509:95 (2015)
81. Frankfurt L, Guzey V, Strikman M, Zhalov M. *Phys. Lett. B* 752:51 (2016)
82. Klein SR. *Proc. Sci.* DIS2016:188 (2016)
83. Abelev BI, et al. *Phys. Rev. C* 81:044901 (2010)
84. Mayer C. *Results (and future prospects) of the ALICE experiment in photon-induced collisions in Pb-Pb collisions*. Workshop presented at CERN, Geneva, June 2–6. **https://indico.cern.ch/event/216417/contributions/1515422/** (2014)

85. Good ML, Walker WD. *Phys. Rev.* 120:1857 (1960)
86. Kowalski H, Motyka L, Watt G. *Phys. Rev. D* 74:074016 (2006)
87. Rezaeian AH, Siddikov M, Van de Klundert M, Venugopalan R. *Phys. Rev. D* 87:034002 (2013)
88. Lappi T, Mantysaari H. *Phys. Rev. C* 87:032201 (2013)
89. Mantysaari H, Schenke B. *Phys. Rev. D* 94:034042 (2016)
90. Guzey V, Strikman M, Zhalov M. *Phys. Rev. C* 95:025204 (2017)
91. Emel'yanov V, Khodinov A, Klein SR, Vogt R. *Phys. Rev. C* 61:044904 (2000)
92. Acharya S, et al. *Phys. Lett. B* 798:134926 (2019)
93. Luszczak A, Schaefer W. *Phys. Rev. C* 99:044905 (2019)
94. Burkardt M. *Int. J. Mod. Phys. A* 18:173 (2003)
95. Toll T, Ullrich T. *Phys. Rev. C* 87:024913 (2013)
96. Miettinen HI, Pumplin J. *Phys. Rev. D* 18:1696 (1978)
97. Frankfurt L, Strikman M, Weiss C. *Annu. Rev. Nucl. Part. Sci.* 55:403 (2005)
98. Cepila J, Contreras JG, Tapia Takaki JD. *Phys. Lett. B* 766:186 (2017)
99. Cepila J, Contreras JG, Krelina M. *Phys. Rev. C* 97:024901 (2018)
100. Agakishiev G, et al. (STAR Collab.) *Phys. Rev. C* 85:014910 (2012)
101. Accardi A, et al. *Eur. Phys. J. A* 52:268 (2016)
102. Lansberg JP, Massacrier L, Szymanowski L, Wagner J. *Phys. Lett. B* 793:33 (2019)
103. Schmidke B. *Ultra-peripheral collisions at STAR*. Presented at the 2019 Meeting of the Division of Particles & Fields of the American Physical Society, Boston, MA, July 29–Aug. 2 (2019)
104. Pire B, Szymanowski L, Wagner J. *Phys. Rev. D* 79:014010 (2009)
105. Klein SR, Xie YP. *Phys. Rev. C* 100:024620 (2019)
106. Yang Q. *Nucl. Phys. A* 982:951 (2019)
107. Brambilla N, et al. arXiv:1907.07583 [hep-ex] (2019)
108. Lin QY, Liu X, Xu HS. *Phys. Rev. D* 89:034016 (2014)
109. Wang XY, Chen XR, Guskov A. *Phys. Rev. D* 92:094017 (2015)
110. Gonçalves VP, da Silva MLL. *Phys. Rev. D* 89:114005 (2014)
111. Gonçalves VP, Jaime MM. *Phys. Lett. B* 805:135447 (2020)
112. Ali A, et al. *Phys. Rev. Lett.* 123:072001 (2019)
113. Adam J, et al. (STAR Collab.) *Phys. Rev. Lett.* 123:132302 (2019)
114. Adam J, et al. (ALICE Collab.) *Phys. Rev. Lett.* 116:222301 (2016)
115. Kłusek-Gawenda M, Szczurek A. *Phys. Rev. C* 93:044912 (2016)
116. Gay Ducati MB, Martins S. *Phys. Rev. D* 97:116013 (2018)
117. Hencken K, Trautmann D, Baur G. *Z. Phys. C* 68:473 (1995)
118. d'Enterria D, da Silveira GG. *Phys. Rev. Lett.* 111:080405 (2013). Erratum. *Phys. Rev. Lett.* 116:129901 (2016)
119. Brodsky SJ, Kinoshita T, Terazawa H. *Phys. Rev. D* 4:1532 (1971)
120. Budnev VM, Ginzburg IF, Meledin GV, Serbo VG. *Phys. Rep.* 15:181 (1975)
121. Baltz AJ, Gorbunov Y, Klein SR, Nystrand J. *Phys. Rev. C* 80:044902 (2009)
122. Baur G, Ferreira LG. *Phys. Lett. B* 254:30 (1991)
123. Afanasiev S, et al. (PHENIX Collab.) *Phys. Lett. B* 679:321 (2009)
124. Abbas E, et al. (ALICE Collab.) *Eur. Phys. J. C* 73:2617 (2013)
125. Adams J, et al. (STAR Collab.) *Phys. Rev. C* 70:031902 (2004)
126. ATLAS Collab. *Measurement of high-mass dimuon pairs from ultraperipheral lead-lead collisions at* $\sqrt{s_{NN}} = 5.02$ *TeV with the ATLAS detector at the LHC*. ATLAS Note ATLAS-CONF-2016-025, CERN, Geneva (2016)
127. Adam J, et al. (STAR Collab.) arXiv:1910.12400 [nucl-ex] (2019)
128. Kłusek-Gawenda M, Szczurek A, Machado MVT, Serbo VG. *Phys. Rev. C* 83:024903 (2011)
129. Sengul M, Guclu MC, Mercan O, Karakus N. *Eur. Phys. J. C* 76:428 (2016)
130. Azevedo C, Gonçalves VP, Moreira BD. *Eur. Phys. J. C* 79:432 (2019)
131. Vysotsky MI, Zhemchugov E. *Phys.-Uspekhi* 62:910 (2019)
132. Zha W, et al. *Phys. Lett. B* 781:182 (2018)

133. Li C, Zhou J, Zhou YJ. *Phys. Lett. B* 795:576 (2019)
134. ATLAS Collab. *2018 heavy ion collision event (365914, 562492194): back-to-back electron-muon pair in an ultra-peripheral collision recorded with the ATLAS detector during the 2018 Pb+Pb data-taking period*. Event Disp. ATLAS-EVENTDISPLAY-2018-009, CERN, Geneva. **http://cds.cern.ch/record/2649465** (2018)
135. Silverman DJ, Shaw GL. *Phys. Rev. D* 27:1196 (1983)
136. Martin SP, Wells JD. *Phys. Rev. D* 64:035003 (2001)
137. Beresford L, Liu J. arXiv:1908.05180 [hep-ph] (2019)
138. Dyndał M, Kłusek-Gawenda M, Schott M, Szczurek A. arXiv:2002.05503 [hep-ph] (2020)
139. Klein S, Mueller AH, Xiao BW, Yuan F. *Phys. Rev. Lett.* 122:132301 (2019)
140. Klein S, Mueller A, Xiao BW, Yuan F. arXiv:2003.02947 [hep-ph] (2020)
141. Sjöstrand T, et al. *Comput. Phys. Commun.* 191:159 (2015)
142. Hencken K, Baur G, Trautmann D. *Phys. Rev. C* 69:054902 (2004)
143. Aste AW. *EPL* 81:61001 (2008)
144. Klein SR. *Nucl. Instrum. Meth. A* 459:51 (2001)
145. Bruce R, Bocian D, Gilardoni S, Jowett JM. *Phys. Rev. ST Accel. Beams* 12:071002 (2009)
146. Jowett J, et al. Bound-free pair production in LHC Pb-Pb operation at 6.37 Z TeV per beam. In *Proceedings of the 7th International Particle Accelerator Conference (IPAC2016)*, ed. KS Kim, IS Ko, KR Kim, VRW Schaa, pp. 1497–500. Geneva: JACoW. **http://accelconf.web.cern.ch/ipac2016/papers/tupmw028.pdf** (2016)
147. Baur G, et al. *Phys. Lett. B* 368:251 (1996)
148. Blanford G, et al. *Phys. Rev. Lett.* 80:3037 (1998)
149. Wells JC, Oberacker VE, Strayer MR, Umar AS. *Phys. Rev. A* 53:1498 (1996)
150. Bertulani CA, Ellermann M. *Phys. Rev. C* 81:044910 (2010)
151. Azevedo C, Gonçalves VP, Moreira BD. *Phys. Rev. C* 101:024914 (2020)
152. Kłusek-Gawenda M, Lebiedowicz P, Szczurek A. *Phys. Rev. C* 93:044907 (2016)
153. Ginzburg IF, Schiller A. *Phys. Rev. D* 57:6599 (1998)
154. Fichet S, et al. *J. High Energy Phys.* 1502:165 (2015)
155. Knapen S, Lin T, Lou HK, Melia T. *Phys. Rev. Lett.* 118:171801 (2017)
156. Bauer M, Neubert M, Thamm A. *J. High Energy Phys.* 1712:44 (2017)
157. Jarlskog G, et al. *Phys. Rev. D* 8:3813 (1973)
158. Akhmadaliev SZ, et al. *Phys. Rev. Lett.* 89:061802 (2002)
159. Aad G, et al. (ATLAS Collab.) *Phys. Rev. Lett.* 123:052001 (2019)
160. Aaboud M, et al. (ATLAS Collab.) *Nat. Phys.* 13:852 (2017)
161. Sirunyan AM, et al. (CMS Collab.) *Phys. Lett. B* 797:134826 (2019)
162. Aad G, et al. (ATLAS Collab.) *Eur. Phys. J. C* 76:210 (2016)
163. Klein SR. *Phys. Rev. D* 98:118501 (2018)

Annual Review of Nuclear and Particle Science

Volume 70, 2020

Contents

Errata

An online log of corrections to *Annual Review of Nuclear and Particle Science* articles may be found at http://www.annualreviews.org/errata/nucl